Numerical study of the interactions between the pile-net aquaculture structures and extreme waves

Gang Wang[1], Ting Cui[2], Bing Tai [*3], Changtao Guan[1], Ahmet Soydan[4], Widar Weizhi Wang[4], and Hans Bihs[4]

[1]State Key Laboratory of Mariculture Biobreeding and Sustainable Goods, Yellow Sea Fisheries Research Institute, Chinese Academy of Fishery Sciences, Qingdao 266071, China
[2]School of Ocean Engineering, Harbin Institute of Technology, Weihai 264209, China
[3]School of Naval Architecture and Ocean Engineering, Jiangsu University of Science and Technology, Zhenjiang 212100, China
[4]Department of Civil and Environmental Engineering, Norwegian University of Science and Technology (NTNU), 7491 Trondheim, Norway

Ocean Engineering, 2026, **348**, pp. 124074.
DOI: https://dx.doi.org/10.1016/j.oceaneng.2025.124074

Abstract

Extreme waves are recognised as the governing loads for pile–net aquaculture structures (PNAS) widely serviced in China, yet the transient impact physics and distinct spectral features of the reciprocal interactions remain poorly quantified. The responses of a classic PNAS to the excitations of focused wave groups are studied using the open-source hydrodynamics toolbox REEF3D. Rigid piles are represented by the direct forcing immersed boundary method, while the responses of nets are modelled using the Lagrangian–Eulerian coupling algorithm. The framework is verified for free surface elevations and validated for impact forces against laboratory measurements. At the most exposed case, when the plunging jet first impinged, simultaneous horizontal peaks on piles and net reached 187.50 and 104.28 kN at full scale. The continuous wavelet transform identifies a broadband frequency excitation and energy spiking at impact. Local loads on the net are 3.72 to 3.87 kN maximally, and rise to about 21.46 kN when the solidities increase from 0.15 to 0.50. The non-linear interactions between the PNAS and extreme waves are further highlighted through the parametric studies, including the placement of the PNAS, wave parameters and net solidities. The findings of this study are expected to update the knowledge for designs and optimisations of the PNAS in the future.

*Corresponding author, taibing@just.edu.cn

Keywords:

Pile-net aquaculture structures (PNAS) ; Hydrodynamics ; Fluid-structure interactions ; Extreme waves ; REEF3D

1 Introduction

Mariculture is currently transitioning from near-shore regions to offshore areas to resolve the conflicts between the increasing demand for high-quality, sustainable protein sources and the limited space available in coastal zones. The advantages of lower pollution and disease levels in open oceans contribute to the large-scale industrial expansion of mariculture, which overwhelms the traditional household farming in near-shore areas. In the course of the expansion, some novel designs and larger constructions in offshore aquaculture structures (OAS) are possible to account for the harsher sea states Chu et al. (2020). Over recent years, the prevalent scheme in OAS is to combine steel piles or trusses and the strengthened net systems through rebars, i.e., reinforcing bars or ropes, as evidenced in Fig. 1. The original intention of this design is to restrict the motion responses of floating farms in strong currents and waves and avoid considerable volume shrinking of the fish enclosure. Especially, the pile-net aquaculture structures (PNAS) are preferred in the Yellow and Bohai seas due to the superior structural strengths of pile column structures and the relatively shallow water depths against other regions in China. As the exemplary pilot projects in China, Jinghai No. 1 bottom-supported smart fish farm (Fig. 1(c)) and Lanzuan No. 1 aquaculture pen (Fig. 1(d)) are primarily constructed from piles and nets. As a representative OAS serviced in Lai-zhou Bay, Bohai Sea, Lanzuan No. 1 aquaculture pen allows for the enclosure of a significant water surface area and optimises the utilisation of vertical water space, making it suitable for open sea areas with gentle continental shelf gradients. It is enclosed by 80 units of circular piles spaced with 5 m intervals and polyethylene terephthalate (PET) nets, resulting in a unit water volume cost as low as 163 CNY per cubic meter and proposing a cost-effective solution for offshore aquacultures.

However, several challenges arise in reality that need to be addressed. It is important to note that established offshore engineering practices, which are often derived from oil and gas platforms or wind turbines, may be more applicable to the structural designs or spatial configurations of steel frames or pile groups than to net systems Wang et al. (2022); Chu et al. (2023). This is significant considering that net systems account for approximately 70% of the exposed areas in OAS Wang et al. (2024). The properties of materials and their stiffness play a crucial role in determining specific guidelines for hydrodynamic evaluations and manufacturing processes Fan et al. (2023); Tavakoli et al. (2025). Wang et al. (2022) has recorded that the existing practical pile–net aquaculture pens in China have experienced various levels of structural failures, including breakage of pile–net joint points, tearing of nets, and pile collapses. These damages have opened up the intriguing research fields to investigate the hydrodynamic characteristics of combined rigid body and net structures, to address the above concerns.

Postprint, published in Ocean Engineering, doi:https://doi.org/10.1016/j.oceaneng.2022.111528

(a) Submersible offshore fish farm Deep Blue No. 2

(b) Semi-submersible offshore fish farm Haiwei No. 2

(c) Bottom-supported smart fish farm Jinghai No. 1

(d) Aquaculture pen Lanzuan No. 1

Figure 1: The representative offshore aquaculture structures featuring pile-net or truss-net structures in China.

Besides, one of the critical challenges in offshore aquacultural engineering is ensuring the survival of OAS under extreme wave conditions in exposed ocean environments. This issue nowadays has been further exacerbated by increased typhoon and storm surge frequencies due to long-term climate change Wang et al. (2021). Extreme waves generally refer to random ocean waves in nature, comprising numerous wave components with varying amplitudes, frequencies and phases. Through nonlinear interactions and superposition amongst these components, extreme waves can emerge unexpectedly, attaining gigantic heights that far exceed predictions derived from the prevailing sea state Kharif (2009); McAllister et al. (2024). Marine structures are subject to tremendous loads Mi et al. (2025) or unforeseen oscillations Gao et al. (2020) by the transient impact of extreme waves. These hydrodynamic characteristics are accompanied by wave breaking, run-up and the substantial generation of spray, as reported in Fig. 2. Therefore, a comprehensive grasp of the hydrodynamics of OAS is vital during the pre-design or optimisation phases, especially for the inclusion of the coupled system of rigid bodies and nets in extreme wave conditions. The consideration of extreme waves can facilitate the establishment of robust design parameters, significantly enhancing the resilience of OAS against the forces imposed by harsh states.

Retrospectively, the hydrodynamics of PNAS or truss-net structures are studied experimentally and numerically. Based on the validation of towing experiments, the resultant tensions of net twines and restrained ropes equipped with a PNAS, as well as their deformations,

(a) (b)

Figure 2: Extreme waves impact on an offshore O&G platform Normannsen (2021) and a bottom-supported fish farm through the live monitoring system.

are studied using the lumped mass method in Wang et al. (2022). A one-way fluid-structure coupling model is later proposed and accounts for the disturbances in flow fields and structural responses of a PNAS in the steady currents Yang et al. (2022). Here, the impacts of different factors including the configurations, inclination angles, distances between double rows and Young's modulus of nets are involved to provide insights for further optimisations. Next, the hydrodynamic interactions between nets and cylinders featuring PNAS or truss-net structures are studied by physical tests Wang et al. (2023) and computational fluid dynamics (CFD) modellings Chen et al. (2024). The hydrodynamic forces on and the flow fields of pure cylinder, pure net, and the combined cylinder-net structure are compared under different inflow angles and net solidities. In order to improve the modelling accuracy and efficiency, a novel numerical framework to model the interactions between the full-scale PNAS and waves is introduced by Zhao et al. (2024), wherein the direct-forcing immersed boundary method and the porous-media model are tailored for the piles and nets coupled with the flow solver, respectively. The three-dimensional non-hydrostatic model NHWAVE in sigma coordinate is used to describe the wave fields. Based on the experimental validation, the dependences of wave periods, net solidities, relative spacings and inclination angles on the regular wave field morphologies are discussed. Moreover, Xie et al. (2025) has paid more attention to the parametric effects of piles and soils using a nonlinear coupled model, and it is revealed that the wave-induced vibrations of the PNAS decrease as the pile diameter increases, the pile length in seabed soil increases, or the seabed soil becomes more rigid. It can be noticed that the existing research focuses on either regular waves or steady currents, which is not reflective of the features of extreme waves. To bridge this gap, the nonlinear interactions between the PNAS and the focused breaking wave are highlighted for the first time Wang et al. (2025), where the input focused breaking wave characterizing extreme waves is modelled using the transient wave packet method. The surging of wave impact forces on the PNAS is correlated with the interplay between the PNAS and the rolling breaker tongues based on the CFD observations.

Although numerous researchers have made progress in addressing the hydrodynamic properties of PNAS or truss-net structures, little effort is paid to the effects of extreme wave conditions. In contrast to regular waves, extreme waves are characterised by distinct spectral features and considerably larger wave heights Kharif (2009); McAllister et al. (2024). The dominant loads imposed on structures pose a significant threat to structural safety. Moreover,

extreme waves are prone to breaking, and the loads imparted to structures differ significantly at different stages of wave breaking Tai et al. (2024). Consequently, hydrodynamic responses of PNAS measured under regular wave or current loads may not extend to such extremes. Despite the fact that some studies have examined the responses of net panels in extreme waves Xu et al. (2021); Chen et al. (2024), comprehensive investigations of PNAS under such impacts are scarce.

The main contribution of this paper is to examine the nonlinear interactions between the PNAS from the Lanzuan No. 1 aquaculture pen and focused waves. For this purpose, the high-fidelity CFD solver of the open-source hydrodynamic framework REEF3D is utilised, incorporating with a continuous direct forcing approach and a Lagrangian–Eulerian coupling algorithm for rigid body and net dynamics. The capacities of using CFD method to study the nonlinear interactions between offshore structures and extreme waves are well established Gao et al. (2024); Mi et al. (2025); Gao et al. (2026). In particular, the NewWave theory proposed by Tromans et al. (1991) provides a well-established deterministic representation of an extreme wave event, corresponding to the average shape of the largest wave event in a Gaussian sea state. It is hence utilised to generate the focused waves. Given on the validation of the numerical framework, the hydrodynamics of the PNAS in scenarios involving the most exposed focused breaking waves, as well as the relevance with wave and structural parameters, are extensively discussed. The clarification of the responses of the PNAS to such excitations will update the knowledge for designs and optimisations of OAS in the future.

2 Numerical framework

In this section, the numerical method to study focused wave interactions with the PNAS is described in detail. Based on the REEF3D platform, the FSI framework is composed of a two-phase numerical wave tank modelling focused waves, rigid body and net dynamics solver as well as the coupling strategy. The disturbances of viscous fluids by rigid bodies and nets are incorporated through two additional forcing terms, which are further formulated by a novel continuous forcing approach and a Lagrangian–Eulerian coupling algorithm, respectively.

2.1 Incompressible viscous flow solver

The conservation laws of mass and momentum of the incompressible viscous fluids in numerical wave tanks (NWT) are preserved by solving the three-dimensional continuity and Navier-Stokes equations, which are given in the convective form

$$\nabla \cdot \mathbf{u} = 0,$$
$$\frac{\partial \mathbf{u}}{\partial t} + (\mathbf{u} \cdot \nabla)\mathbf{u} = -\frac{1}{\rho}\nabla p + \nabla \cdot \left[(\nu + \nu_t)\left(\nabla \mathbf{u} + (\nabla \mathbf{u})^\top\right)\right] + \mathbf{g} + \mathbf{R} + \mathbf{N}. \tag{1}$$

where $\mathbf{u}$ represents the velocity vector, ρ is the fluid density, ∇p represents the pressure gradient term, $\mathbf{g}$ is the gravity acceleration vector, $\mathbf{R}$ and $\mathbf{N}$ denote the forcing terms characterising momentum loss due to rigid bodies and nets. ν equals the kinematic viscosity while the eddy viscosity ν_t accounts for the unresolved turbulent stresses term. Building on the Boussinesq approximation, ν_t is then determined by a turbulent kinetic energy k and specific dissipation ω two-equation model Wilcox (1998) with a limiter for ν_t Durbin (2009) and an efficient

approximation of specific dissipation at the free surface ω_s. These closures have mitigated excessive turbulence generation in highly strained flow regions beyond the boundary layer, thereby rendering more accurate predictions of turbulent intensities at the free surface Bihs et al. (2016).

To distinguish the fluid phase from the air phase, the zero level set of a smooth signed distance function Φ is introduced in an implicit manner Osher and Sethian (1988). The temporal and spatial discretisation of Φ can be achieved through an advection equation as presented in Eq. 2, while an additional reinitialisation procedure is subsequently incorporated to ensure the signed distance properties of Φ Sussman et al. (1994)

$$\begin{aligned} \frac{\partial \Phi}{\partial t} + \mathbf{u} \cdot \nabla \Phi = 0, \\ \frac{\partial \Phi}{\partial t} + S(\Phi)\left(|\nabla \Phi| - 1\right) = 0. \end{aligned} \tag{2}$$

here, $S(\Phi)$ is the smooth sign function Peng et al. (1999). The validity of the Eikonal equation $|\nabla \Phi| = 1$ can then be satisfied throughout the entire domain. The density and viscosity of the two-phase flow (ρ_f and ν_f) are calculated at the cell centre using the smoothed Heaviside step function $H(\Phi)$ as

$$\begin{aligned} \rho_f &= \rho_w H(\Phi) + \rho_a (1 - H(\Phi)), \\ \nu_f &= \nu_w H(\Phi) + \nu_a (1 - H(\Phi)) \end{aligned} \tag{3}$$

with

$$H(\Phi) = \begin{cases} 0 & \text{if } \Phi < -\epsilon, \\ \frac{1}{2}\left(1 + \frac{\Phi}{\epsilon} + \frac{1}{\pi}\sin\left(\frac{\pi\Phi}{\epsilon}\right)\right) & \text{if } |\Phi| \leq \epsilon, \\ 1 & \text{if } \Phi > \epsilon, \end{cases} \tag{4}$$

where the subscripts w and a correspond to the properties of water and air, respectively. ϵ gives the thickness of the smoothed out interface equalling $2.1\Delta x$. For more details on the implementation and justification of turbulence modelling and free surface capturing, readers are referred to Bihs et al. (2016).

The aforementioned equations are solved on the staggered structured rectilinear grids using the finite difference method, thus making a tight correlation of the pressure and velocity fields. The fifth-order accurate weighted essentially non-oscillatory (WENO) scheme Jiang and Shu (1996) is used for velocity derivatives, while the Hamilton–Jacobi variant of the WENO scheme Jiang and Peng (2000) is performed for the discretisation of Φ. The second-order accurate central difference scheme is used for the spatial discretisation of the diffusive terms. Moreover, an explicit third-order accurate low-storage Runge-Kutta scheme Spalart et al. (1991) is employed for the temporal advancement of the momentum and level set functions for the free surface (Eq. 2), yet the diffusive term is treated with the first-order Euler scheme implicitly. By decoupling the stability criterion from the $\mathcal{O}(\Delta x^{-2})$ dependency in conventional Courant–Friedrichs–Lewy (CFL) conditions, the present discretisation framework guarantees rigorous numerical stability across arbitrary mesh resolutions Bihs et al. (2016). The forcing terms instigated by rigid bodies and nets need to be included in Eq. 1. The incremental pressure-correction algorithm proposed by Timmermans et al. (1996) is applied to update the

pressure and velocity terms: in the $(j+1)$th sub-step of the Runge-Kutta scheme, the predictor step is added to estimate the pseudo velocity field u^* based on the pressure and velocity terms from the previous jth step. The governing equation for this prediction is reformulated as

$$\frac{\mathbf{u}^* - \mathbf{u}^{(j)}}{\Delta t} = 2\alpha_{(j+1)}\nu\nabla\cdot\left(\left[\left[\nabla\mathbf{u} + (\nabla\mathbf{u})^\top\right]\right]\right)^{(j)} - 2\alpha_{(j+1)}\nabla\left(\frac{p^j}{\rho}\right) - \gamma_{(j+1)}\mathbf{u}^j\cdot\nabla\mathbf{u}^j - \delta_{(j+1)}\mathbf{u}^{j-1}\cdot\nabla\mathbf{u}^{j-1} + \mathbf{g}^* + \mathbf{R}^* + \mathbf{N}^*. \tag{5}$$

where $j = 1, 2, 3$, $\alpha_j = 4/15, 1/15, 1/6$, $\gamma_j = 8/15, 5/12, 3/4$ and $\delta_j = 0, -17/60, -5/12$, respectively. Further, a corrector step for the pressure is then added by solving the following Poisson equation with $\mathbf{u}^*$

$$\nabla\cdot\left(\frac{1}{\rho}\nabla p_{corr}\right) = \frac{1}{2\alpha_{(j+1)}\Delta t}\nabla\cdot\mathbf{u}^*. \tag{6}$$

This equation can be solved using a fully parallelised BiCGStab solver with geometric multigrid preconditioning implemented in the HYPRE library Van Der Vorst (1992). Finally, the updated pressure field and divergence-free velocity field are computed as shown in Eq. 7. An n-halo decomposition strategy combined with the message passing interface (MPI) is implemented, enhancing its applicability and facilitating inter-processor communication during numerical modelling.

$$\begin{aligned} p^{(j+1)} &= p^{(j)} + p_{corr} - \rho\nu\nabla\cdot\mathbf{u}^*, \\ \mathbf{u}^{(j+1)} &= \mathbf{u}^* - \frac{2\alpha_{(j+1)}}{\rho}\Delta t\nabla p^{(j+1)}. \end{aligned} \tag{7}$$

2.1.1 Extreme wave generation, breaking and absorption

As the dispersive focusing technique Longuet-Higgins (1974) is the straightforward approach to generate extreme waves, superimposing component waves of different frequencies at a specific location is used in this study. The linear wave elevation $\eta^{(1)}(x,t)$ is expressed as

$$\eta^{(1)}(x,t) = \sum_{i=1}^{N} a_i\cos\left[k_i\left(x - x_f\right) - \omega_i\left(t - t_f\right)\right]. \tag{8}$$

Here, a_i, k_i and w_i are the amplitude, wave number and angular frequency of each component, respectively. x_f and t_f are the targeted focusing location and time. It can be observed that the free surface elevation can be given as long as a_i is determined. Based on the NewWave theory, a_i is then calculated in relation to the pre-defined focusing amplitude a_f and the spectrum of each harmonic $S_i(\omega)$ as

$$a_i = a_f\frac{S_i(\omega)\Delta\omega}{\sum_{i=1}^{N} S_i(\omega)\Delta\omega}. \tag{9}$$

with

$$\Delta\omega = \frac{\omega_e - \omega_s}{N}. \tag{10}$$

where ω_s and ω_e are the starting and ending bounds of angular frequencies. The total energy of the wave spectrum is distributed to the sub-spectrum characterised by angular frequencies, wherein the peak enhancement method (PEM) is handled for the frequency discretisation. Bounded at the peak frequency ω_p, the entire frequency band can be decomposed into two sub-bands $[\omega_s, \omega_p]$ and $[\omega_p, \omega_e]$ with N_s and N_e components, individually. The even distribution of the frequency harmonics can be ensured while rendering ω_p fixed Wang et al. (2021). The relationship amongst the above parameters reads as

$$\frac{N_s}{N_e} = \frac{\omega_p - \omega_s}{\omega_e - \omega_p}. \tag{11}$$

The Pierson-Moskowitz (PM) spectrum Pierson and Moskowitz (1964) for the fully developed sea state accounts for the generation of the irregular focused waves, given by

$$S(\omega) = \frac{5}{16} H_s^2 \omega_p^4 \omega^{-5} \exp\left\{ -\frac{5}{4} \left(\frac{\omega}{\omega_p} \right)^{-4} \right\}. \tag{12}$$

with

$$\omega_p = \frac{2\pi}{T_p}. \tag{13}$$

where H_s accounts for significant wave heights. In addition, it is imperative to include the second-order implications in the wave elevations and particle velocities, particularly when addressing breaking waves with notable steepness and wave-wave interactions. Building on the second-order irregular wave theory proposed by Schäffer (1996), the free surface elevations η and three-dimensional particle velocities for focused waves can be expressed through the superposition of the linear and second-order components. Further information about the implementations and applicability can be obtained from Ning et al. (2009).

2.2 Rigid body dynamics solver

In the context of level set method and ray-casting algorithm Bihs and Kamath (2017), the rigid body is identified as the signed distance field Φ_s characterised by a Stereolithography (STL) triangular-mesh file. The density and viscosity across the whole domain can be expanded afterwards from Eq. (3) as

$$\begin{aligned} \rho &= \rho_s H(\Phi_s) + (1 - H(\Phi_s)) \cdot (\rho_w H(\Phi) + \rho_a (1 - H(\Phi))), \\ \nu &= (1 - H(\Phi_s)) \cdot (\nu_w H(\Phi) + \nu_a (1 - H(\Phi))). \end{aligned} \tag{14}$$

Here, $H(\Phi_s)$ presents the smooth Heaviside step function of Φ_s as Eq. (4). An enhanced continuous treatment for densities between the fluid and solid phases is enabled and briefed in A.

The disturbances of velocity and pressure fields owing to the presence of rigid bodies are modelled through the direct forcing immersed boundary method (DF-IBM), describing the addend $\mathbf{R}$ at the right-hand of Eq. (1). Based on the deduction in Yang (2018) and the further development in Martin et al. (2021), the formula of $\mathbf{R}$ at the updated step $j+1$ is provided as

$$\mathbf{R}^{(j+1)} = H\left(\Phi_s^{(j+1)}\right) \cdot \left(\frac{\tau\left(\mathbf{u}^{(j+1)}\right) - \mathbf{u}^{(j)}}{\Delta t} + \mathbf{u}^{(j)} \cdot \nabla \mathbf{u}^{(j)} + \frac{1}{\rho} \nabla p^{(j+1)} - \mathbf{g} \right). \tag{15}$$

with τ a divergence-free rigid body velocity field projected from velocities of viscous fluids. The pseudo velocity field $\mathbf{u}^*$, deriving from Eq. (5) without forcing terms, is incorporated before advancing to the Runge-Kutta sub-step $j+1$, and the unknown Φ_s and τ at the updated step $j+1$ are also estimated using $\mathbf{u}^*$ Martin et al. (2021). With reference to Eq. (5), the forcing term based on $\mathbf{u}^*$ can be rewritten as

$$\mathbf{R}^* = H\left(\Phi_s^*\right) \cdot \left(\frac{\tau\left(\mathbf{u}^*\right) - \mathbf{u}^*}{2\alpha_{(j+1)}\Delta t} \right). \tag{16}$$

which is communicated to the predicted velocity field before updating pressure fields (Eq. (6)).

The wave forces $\mathbf{F_w}$ and moments $\mathbf{M_w}$ imposed on rigid bodies can be calculated through the integration of fluid forces over the structure with M triangles in STL file:

$$\begin{aligned} \mathbf{F_w} &= \sum_{k=1}^{M} (-\mathbf{n}p + \rho\nu\mathbf{n}\zeta)_k \cdot \Delta\Omega_i, \\ \mathbf{M_w} &= \sum_{k=1}^{M} \mathbf{r}_i \times (-\mathbf{n}p + \rho\nu\mathbf{n}\zeta)_k \cdot \Delta\Omega_i. \end{aligned} \tag{17}$$

Here, $\mathbf{n}$ is the surface normal vector, ζ is the stress tensor, $\Delta\Omega_i$ equals the area of each triangle and $\mathbf{r}$ gives the distance vector from each element to the centre of gravity.

2.3 Net dynamics solver

In this section, the net dynamics solver accounts for the estimation of exerted wave loads and the modelling of momentum loss of fluids caused by nets. The hydrodynamic forces $\mathbf{H}$ acting on net structures are modelled through three distinct components: drag forces $\mathbf{H}_d$, lift forces $\mathbf{H}_l$ and inertial forces $\mathbf{H}_i$. Due to the prohibitive computational cost of directly integrating hydrodynamic pressure across millions of net twines, the screen force model Kristiansen and Faltinsen (2012) is employed to estimate these forces. In this approach, the net panel is discretised into L screen elements, each representing physical twines and knots. The total hydrodynamic force is calculated by aggregating contributions from all elements through vector summation. For each element with projected area A, the drag and lift forces are computed following the relative flow velocity $\mathbf{u}_{rel}$ and its normal $\mathbf{n}_n$ and tangential $\mathbf{n}_t$ directional vectors. These forces are governed by

$$\begin{aligned} \mathbf{H}_d &= \frac{1}{2}\rho_w C_d A \left|\left|\mathbf{u}_{rel}\right|\right|^2 \mathbf{n}_n, \\ \mathbf{H}_l &= \frac{1}{2}\rho_w C_l A \left|\left|\mathbf{u}_{rel}\right|\right|^2 \mathbf{n}_t. \end{aligned} \tag{18}$$

where C_d and C_l are the drag and lift coefficients fitted by the screen force formulae, respectively. The inertial component accounts for added mass effects through

$$\mathbf{H}_i = m_a \left[\mathbf{a}_f + \begin{pmatrix} \mathbf{n_x} & 0 & 0 \\ 0 & \mathbf{n_y} & 0 \\ 0 & 0 & \mathbf{n_z} \end{pmatrix} \mathbf{a}_{rel} \right]. \tag{19}$$

with m_a the added mass of each screen element, $\mathbf{a}_f$ the fluid particle acceleration, and $\mathbf{a}_{rel}$ the acceleration due to the relative motions of structures with fluids. The cumulative hydrodynamic force $\mathbf{H}$ acting on the entire net panel is thus expressed as:

$$\mathbf{H} = \sum_{k=1}^{L} \left(\mathbf{H}_d^{(k)} + \mathbf{H}_l^{(k)} + \mathbf{H}_i^{(k)} \right). \tag{20}$$

This formulation effectively balances computational efficiency with physical accuracy, enabling practical simulation of complex fluid-net interactions Martin et al. (2020). The spatial distribution of force vectors and mesh discretisation strategy are detailed in prior studies, which can be referred from Kristiansen and Faltinsen (2012). Moreover, the hydrodynamic coefficients C_d and C_l are of great interest to scholars due to the critical dependence on net solidity S_n, Reynolds number Re, inclination angle θ and supplementary geometric parameters. These relationships have been comprehensively examined through experimental and numerical investigations, wherein the Fourier harmonic decomposition methodology raised by Kristiansen and Faltinsen (2012) is prevalent as its rigorously validated accuracy and broad applicability across experimental conditions. Martin et al. (2020) elaborated the formulae with the upgraded Fourier coefficients using a multidimensional optimisation method with bounded constraints. The expressions read as follows

$$\begin{aligned} C_d(\theta) &= c_{d,0} \left(0.9725 \cos\theta + 0.0139 \cos 3\theta + 0.0136 \cos 5\theta\right), \\ C_l(\theta) &= c_{l,\frac{\pi}{4}} \left(1.4500 \sin 2\theta + 0.0537 \sin 4\theta + 0.0004 \sin 6\theta\right) \end{aligned} \tag{21}$$

where the calculations of $c_{d,0}$ and $c_{l,\frac{\pi}{4}}$ can be derived from Kristiansen and Faltinsen (2012) based on their dependencies on S_n and Re. One can be noted that the determinations of force coefficients in Eq. 21 are based on the undisturbed freestream velocity $\mathbf{u}_0$, which can be formulated with $\mathbf{u}_{rel}$ based on Froude's momentum equilibria theory as

$$\mathbf{u}_0 = \frac{C_d(\mathbf{u}_0)}{2\left(\sqrt{1 + C_d(\mathbf{u}_0)} - 1\right)} \mathbf{u}_{rel}. \tag{22}$$

where $\mathbf{u}_0$ can be approximated using the Newton–Raphson method with $\mathbf{u}_0 = \mathbf{u}_{rel}$ at the first step Martin et al. (2020).

On the other hand, the coupling of the hydrodynamics of nets with the flow solver is established on the Lagrangian characterisation of nets within the Eulerian fluid domain Martin et al. (2021). The Lagrangian points are rather distributed uniformly on the net surface, irrespective of the physical twines and knots. The forcing term $\mathbf{N}$ is formed over L_n Lagrangian markers, on the basis of the assignments of hydrodynamic forces $\mathbf{H}$, the gravitational force $\mathbf{G}$, and the buoyancy $\mathbf{B}$ at the fluid cell point (x_i,y_i,z_i), as

$$\mathbf{N} = \sum_{L=1}^{L_n} \frac{(\mathbf{H} + \mathbf{G} + \mathbf{B})_L}{\Delta x \Delta y \Delta z} \, \mathrm{D}\left(\frac{x_i - x_L}{\Delta x}\right) \, \mathrm{D}\left(\frac{y_i - y_L}{\Delta y}\right) \, \mathrm{D}\left(\frac{z_i - z_L}{\Delta z}\right) \tag{23}$$

Here, the forces of a subset of screen elements are lumped on Lagrangian markers. The kernel D Peskin (1977) featuring the distance between the fluid cell point (x_i,y_i,z_i) and the Lagrangian marker is defined as

$$D(x) = \begin{cases} \dfrac{1}{4}\left(1 + \cos\left(\dfrac{\pi x}{2}\right)\right) & \text{if } |x| < 2.0, \\ 0 & \text{if } |x| \geq 2.0. \end{cases} \tag{24}$$

3 Computational details

3.1 Investigated structures, computational domain and grids

As illustrated in Fig. 3(a), the alternating placement of circular steel piles and PET net sheets constitutes the basic unit of "Lanzuan No. 1" aquaculture pen. The side-by-side circular piles and the centrally enclosed PET net panel are defining features of the classic PNAS, and it is chosen as the investigated structures in this work (see Fig. 3(b)). The moderate stiffness of PET twines lead to the enhanced structural integrity of the whole net panel, which is further firmly mounted on the rebars, steel trusses or piles using ropes. The deformations due to waves and currents can thus be deemed negligible against the structural behaviour of piles. Besides, the rigid assumption is conservative for estimating the occurring loads, since the impact energy can be absorbed by the structural deformation Lader et al. (2007); Van Nuffel et al. (2012). It is decided to neglect the deformation of PET nets, enabling a one-way fluid-structure coupling to improve the computational efficiency. The geometric properties of PET nets are primarily expressed in terms of dimensionless solidity ratios S_n as

$$S_n = \frac{A_{pj}}{A}. \tag{25}$$

where A_{pj} is the projected area of twines and A denotes the outline area. For the further consideration of experimental validation in future studies, the investigated PNAS characterising aquaculture pens and bottom-supported fish farms is scaled with the Froude scaling ratio $\lambda = 13.66$ in this paper, except for the PET net twines. This decision is attributed to the difficulties associated with geometrically scaling the dimensions and elastic properties of net twines in comparison to full-scale piles and nets, but keeping the net solidity identical during conversions. The primary structural parameters of the PNAS are also briefed in Fig. 3(b) and Table 1 for further details.

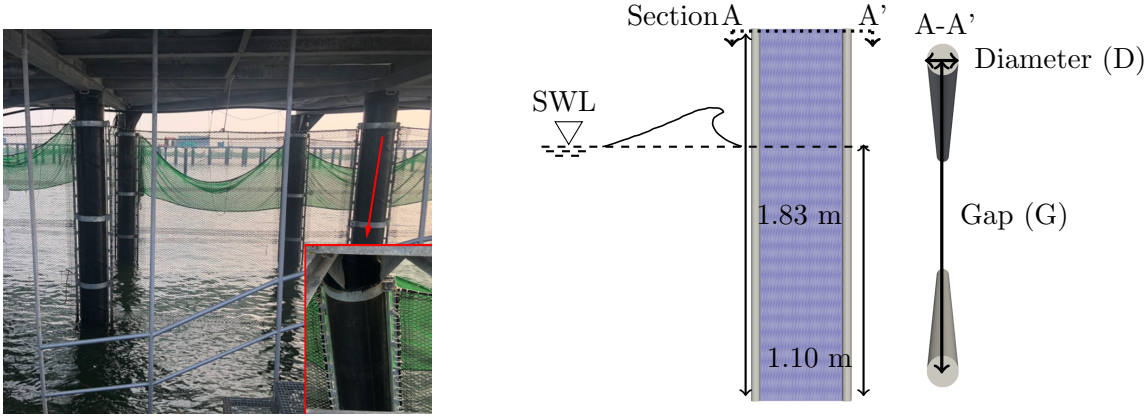

(a) Prototype

(b) Structural model

Figure 3: Overview of the prototype and structural model of PNAS of "Lanzuan No. 1" aquaculture pen.

Table 1: Parameters of the full-scale and model-scale PNAS.

Description	At full scale	At model scale	Unit
Overall height (H)	25.00	1.83	m
Water depth (h)	15.00	1.10	m
Diameter (D)	50.80	3.72	cm
Gap (G)	5.08	0.37	m
Net solidity (S_n)	0.15	0.15	[-]

The investigated PNAS model is placed in a 20.00 m $\times$ 1.00 m $\times$ 2.00 m NWT, with a distance X_0 to the wave entrance and keeping in the middle position over y-axis (see Fig. 4). The interference from lateral boundaries can be overlooked due to the assumed symmetry conditions, which imply that there is no gradient and that particle velocities are normal to the wall. Given that the relaxation method Jacobsen et al. (2012) is of limited applicability for the modelling of non-linearity of steeper waves Wang et al. (2019), the Dirichlet method imposing the velocity properties is adopted for wave generations, while the focused wave past structures are finally damped using the active wave absorption (AWA) method Schäffer and Klopman (2000) at the numerical beach. The combination of Dirichlet and AWA methods for wave generations and damping has been previously justified and applied for focused breaking wave cases in Bihs et al. (2019). In order to capture the significant wave structure interactions as well as the evolution of wave focusing and breaking, the uniformly-sized gridding zone for 6.00 m $\times$ 0.70 m in the x-z plane is enabled around PNAS, and the grid size is subsequently determined based on the independence study and the experimental validation in Section 4. The grids outside the refinement zone are stretching linearly with the factor of 1.10 except for the grids in the y-axis, until the maximum grid size 0.016 m is attained.

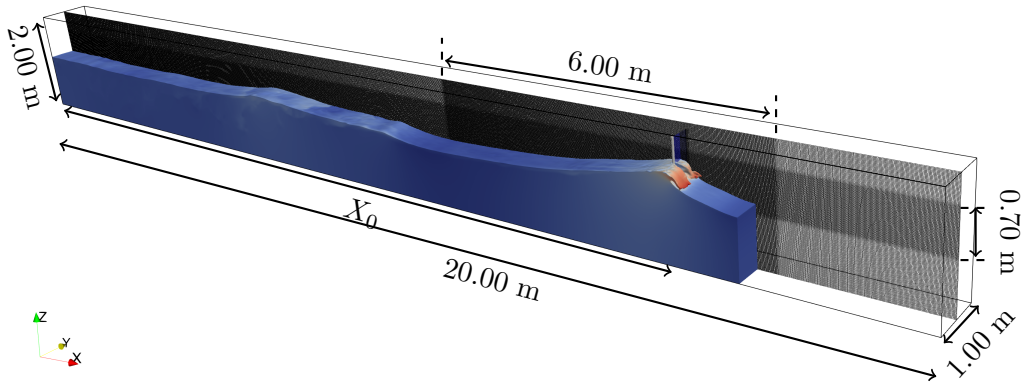

(a) Computational domain and far-field grids

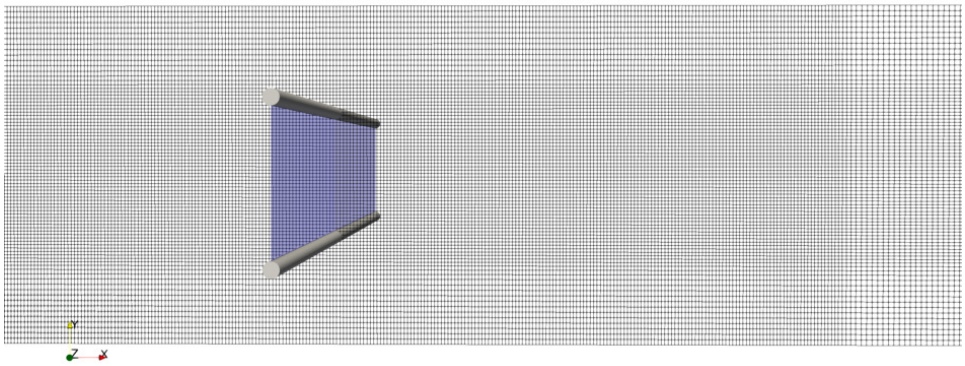

(b) Near-wall grids

Figure 4: Overview of the computational domain and grids.

3.2 Load conditions

The load cases outlined in Table 2 are intended to examine the hydrodynamics of PNAS concerning focused wave parameters, breaker tongue locations, and structural variations. A1 - A9 refer to the wave cases in Zhu et al. (2023), ensuring a better numerical replication of focused waves under the experimental conditions. The prescribed wave focusing amplitudes a_f vary from 0.08 to 0.40, as specified in A1 - A4 and A8 - A9 while keeping other parameters unchanged. It is noteworthy that the full-scale prescribed a_f after Froude conversion is in accordance with the long-term field observations around "Lanzuan No. 1" pen in Lai-zhou Bay Liu (2020). The peak frequencies f_p considered as a crucial parameter for identifying the extreme wave spectrum are within 0.35 to 0.50 Hz. $k_p a_f$ gives the wave steepness where

k_p is the wave number associated with f_p. Based on the breaking index formula proposed by Goda (2010) and the physical observations in Zhu et al. (2023), A1 - A7 are classified as the non-breaking waves while A8 - A9 are located on the breaking scenarios. The focusing location x_f is 14.80 m for all load cases, respectively. B1 - C5 are established for studying the effects of breaker tongue locations and net solidities under a focused breaking wave loading.

Table 2: Load cases

Cases	Focused wave parameters				X_0 [m]	S_n of nets [-]
	a_f [m]	f_p [Hz]	$k_p a_f$	x_f [m]		
A1	0.08	0.40	0.07			
A2	0.10	0.40	0.09			
A3	0.12	0.40	0.10			
A4	0.15	0.40	0.13			
A5	0.12	0.50	0.14	14.80	16.00	0.15
A6	0.12	0.45	0.12			
A7	0.12	0.35	0.09			
A8	0.32	0.40	0.27			
A9	0.40	0.40	0.34			
B1					13.00	
B2					14.00	
B3	0.40	0.40	0.34	14.80	15.00	0.15
B4					17.00	
B5					18.00	
C1						0.10
C2						0.20
C3	0.40	0.40	0.34	14.80	16.00	0.30
C4						0.40
C5						0.50

3.3 Data processing method

In this section, the tilde symbol is adopted to denote non-dimensional quantities, and the non-dimensionalised impact loads on piles $\tilde{F_p}$ and nets $\tilde{F_n}$ are given to facilitate further data analyses as

$$\begin{aligned} \tilde{F_p} &= F_p / \left(\rho D H_w {U_{wc}}^2\right), \\ \tilde{F_n} &= F_n / \left(\rho G H_w S_n {U_{wc}}^2\right). \end{aligned} \tag{26}$$

where H_w is the vertical height from the wave crest to the subsequent trough and U_{wc} is the wave propagating velocity at the crest condition. DH_w and GH_wS_n represent the projected areas of piles and nets exposed to the focused wave with the wave height H_w, respectively.

The evolution of focused waves or the subsequent overturning and collapses at the PNAS remain the inherent transient, non-periodic and non-linear properties, showing the occasional high peaks marking an otherwise relatively undisturbed signal. It should be noted that the typical Fourier-based method can only provide the frequency-spectrum information based on the averaging processing on periodic signals, whereas the deficiencies in spatial or temporal local patterns of non-stationary oscillated signals are quite evident Huang et al. (1998). A possible remedy in recent years lies in the continuous wavelet transform (CWT) Lin and Liu (2004). In Ma et al. (2009), the non-breaking wave impact forces on piles are processed

with the CWT method, so the non-linear, transient and local features of non-stationary force signals over the time and frequency domains are successfully decoded. Later, the subjected pressures generated by the plunging breaker on piles and columns are further analysed in Tai et al. (2024) and Zhang et al. (2025), wherein the local pressures at certain points distributed on piles and columns are closely associated with the evolution of the breaker tongue and the impacting stages. As a baseline, the $WT(s,t)$ of a discrete time sequence $y_n(t)$ is formulated as

$$WT(s,t) = \sum_{n=0}^{N-1} y_n(t)\psi^* \left[\frac{\left(n-n^{'}\right)\Delta t}{s}\right]. \tag{27}$$

where the * symbol gives the complex conjugate, $n^{'}$ denotes the translation of the wavelet function relative to the original signal along the time axis, N is the discrete number of sampling points, s is the wavelet scaling parameter that can be approximated as the inverse of frequencies Ma et al. (2009). ψ is derived based on the nondimensionalisation of the basic wavelet function ψ_0, which can be re-formulated as

$$\psi\left[\frac{\left(n-n^{'}\right)\Delta t}{s}\right] = \left(\frac{\Delta t}{s}\right)^{1/2}\psi_0\left[\frac{\left(n-n^{'}\right)\Delta t}{s}\right]. \tag{28}$$

where ψ_0 is determined based on the Morlet wavelet Lin and Liu (2004), which is commonly recognised as one of the most prevalent CWT methods. It is a complex plane wave modulated by a Gaussian envelope, exhibiting good localisation in both the time and frequency domains. ψ_0 can be written as

$$\psi_0 = \pi^{-1/4}\exp\left(-\frac{t^2}{2}\right)\exp\left(i\omega_0 t\right). \tag{29}$$

where ω_0 is the central frequency which is usually chosen 6.0 to meet the admissibility condition Farge (1992). Finally, the wavelet energy spectrum can be calculated as Eq. 30, and the interested readers can refer to Tai et al. (2019) for more detailed elaborations.

$$W(s,t) = \frac{WT(s,t)WT^*(s,t)}{s}. \tag{30}$$

4 Validation of the numerical method

4.1 Verification of wave profiles

Firstly, the accuracies of the NWT for focused wave generations are verified based on the independence examinations of computational grids and CFL numbers, and the simulated free surface elevations are also compared against the measured data in Zhu et al. (2023). Here, the hydrodynamics of a point-absorbing wave energy converter model in focused waves are measured in a 1.1 m depth wave tank, wherein the motion responses, induced mooring restoring forces as well as surface elevations at several locations are obtained. A two-dimensional case of A9 is simulated without the PNAS to perform a grid independence examination, and the targeting wave gauge is located at the pre-defined $x_f = 14.80$ m. The computational domain

and grid refinement strategy remain consistent with the aforementioned conditions. Four gridding sizes ranging from 0.008 m to 0.014 m are involved. The comparisons between the numerical and experimental time variations of free surface elevations are depicted in Fig. 5. It can be observed that the temporal evolutions of surface elevations are irrespective of the studied sizes of grids, aside from minor variations at some crests and valleys. From the enlarged details in Fig. 5(a), the decent approximation to the theoretical $a_f = 0.40$ m is the case with $dx = 0.010$ m. A good agreement of the synchronisation of phases between the numerical and experimental results can be shown, but the distinction lies in magnitudes instead. It might be attributed to the non-linear interactions between floating bodies and focused waves at the focal point in the experimental situation, along with the numerical dissipation introduced by discretised schemes in CFD calculations. From Fig. 5(b), the independences of free surface elevations and CFL numbers can be confirmed with $dx = 0.010$ m.

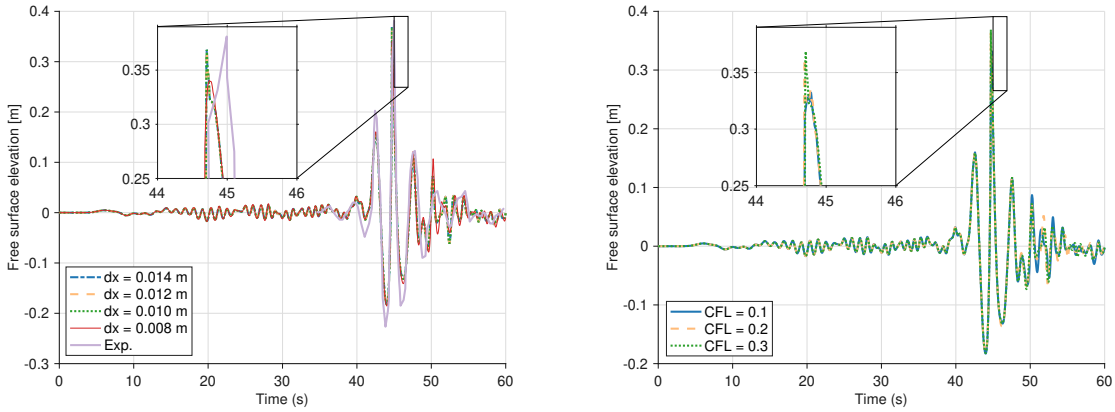

(a) Computational grids

(b) CFL numbers

Figure 5: Numerical and experimental time instances of free surface elevations for examining the independences of computational grids and CFL numbers.

From the perspective of qualitative demonstration (see Fig. 6), the evolution process of the focused plunging wave is illustrated using $dx = 0.010$ m. The wave crest is identified as the occurrence of the vertical wavefront through propagation Bonmarin (1989), and it is focused through the interaction of each harmonic component. Next, the overturning breaker tongue becomes the dominant feature as the horizontal velocities of wave particles rapidly accelerate in between. For the plunging wave-breaking, it is the typical criterion to recognise the onset of breaking as the moment the wave crest begins to turn over Carini et al. (2021). In the third phase, the tongue continues to roll and transform, eventually impinging on the free surface and creating a trapped air cavity. The initial impingement between the breaker tongue and wave surfaces triggers the splash-up of water jets, due to the minor loss of fluid momentum. This can be manifested by the distributions of horizontal velocities in Fig. 6. Finally, the evolvement of wave breaking is followed by a secondary clockwise rolling and a significant splash-up in the counter-clockwise direction. The energy concentrated within the focused waves is ultimately dissipated, resulting in a reduction in the horizontal velocities of the wave particles. The comparable phenomena are also reported in Lim et al. (2015) via the experimental observation. The validity of the modelled wave focusing and breaking is thus

justified initially. As a consequence, all simulations across the paper are conducted using the optimised grid size $dx = 0.010$ m and CFL number 0.3, balancing the numerical accuracies and stabilities.

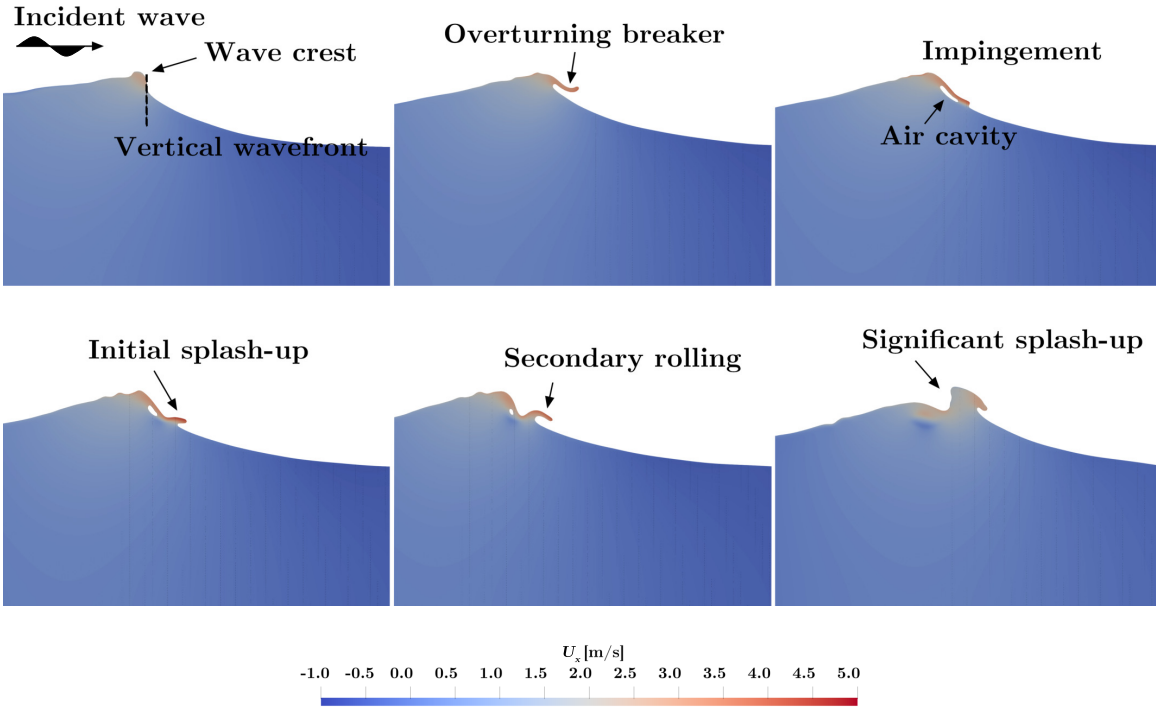

Figure 6: Evolution process of the focused breaking wave using the grid size $dx = 0.010$ m.

4.2 Validation of wave impact forces on the PNAS

The accuracy of wave impact forces on the PNAS using the current FSI framework is validated in this section. In the published experimental works Yang et al. (2022); Zhao et al. (2024), the hydrodynamics of PNAS are evaluated in regular waves or currents rather than focused waves, not to mention the NewWave theory for wave generation. Thus, the validation process concentrates on the comparisons of the impact forces on the circular cylinder and the net panel separately.

In Tai et al. (2019), the experiments on different evolved stages of a plunging breaker impacting a vertical cylinder have been conducted in finite water depth, and it is reproduced numerically in this work. Here, the test cylinder with the height 0.65 m and the diameter 0.06 m is installed in a 22.00 m $\times$ 0.45 m $\times$ 0.60 m wave flume. The focused plunging wave is prescribed with the constant steepness spectrum and the dispersive focusing method, which is composed of 64 sinusoidal linear components ranging from 0.3 Hz to 2.0 Hz. The resultant linear summation of the wave amplitude and the steepness are 12.12 cm and 0.48 in that order. The pre-defined x_f and a_f are assigned as 9.30 m and 0.07 m, respectively. Based on the same experiments, Cui et al. (2022) has modelled the impact forces on the cylinder when the overturning breaker strikes the structure after the crest situation, using the comparable numerical framework in REEF3D. A satisfactory agreement between the

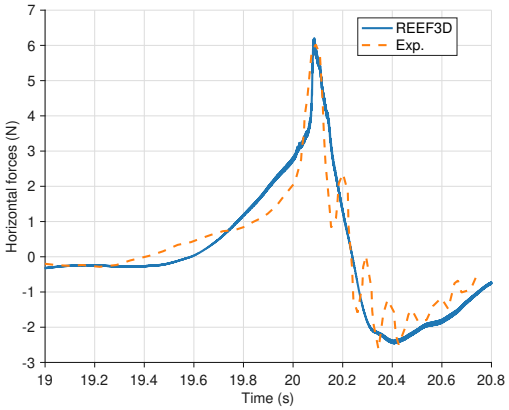

Figure 7: Numerical and experimental time series of the wave impact force on the pile with $X_0 = 9.50$ m.

numerical and experimental exerted forces has been presented with the relative error less than 5%. It should be noticed that the current method has been enhanced for the temporal advancement, as the momentum and level set equations for the free surface are explicitly advanced in a coupled manner, which is not considered in the previous study. Therefore, another validation is carried out for the PNAS placed with a 9.50 m distance to the inlet. It corresponds to the occasion when the plunging jet is curled down and impinges on the free surface at the cylinder face. The comparisons between the numerical and experimental wave impact forces on the pile with $X_0 = 9.50$ m over time are provided in Fig. 7. It can be observed that the envelopes of the numerical and physical results align well, particularly for the phase and the peak force amplitude around the wave focusing moment. The relative error of the peak force amplitude keeps approximately 2.72%. However, the distinctions still occur for the rising rates of the exerted forces ahead of the focusing moment, and the oscillations of the experimental data within 20 s - 20.8 s cannot be seen in the simulations. The reason might be the numerical treatment of the cylinder compared to the experimental condition, as addressed in Tai et al. (2019). The physical cylinder placed in the wave flume is elastic and can oscillate with a high frequency in steep or breaking waves, namely the "ringing" phenomenon Chaplin et al. (1997). This cannot be reproduced numerically as the elastic response is not considered in the fixed case of the cylinder. Besides, the significant mixture of water and air, which is closely related to energy concentrations and dissipations, leads to the development of wave focusing and breaking. The differences in energy transportation can be introduced as the usage of RANS modelling compared to the physical examination.

Next, the capability of estimating the wave impact forces on nets using the current solver is justified using the measured data of net panels in focused waves Chen et al. (2024). An ultra-high molecular weight polyethylene (UHMWPE) net panel of 40.00 cm × 50.00 cm is secured at four corners with a steel frame, then fixed in the centre of 22.00 m (length) × 0.45 m (width) × 0.40 m (water depth) wave flume of Dalian University of Technology. The panel remains 14.50 cm above the still water level (SWL) to ensure the wave crest can fully interact with net twines. The incident wave is also modelled via the constant steepness method, which is composed of 51 regular wave harmonics of 0.5 Hz - 1.5 Hz. The steepness of all harmonics

in this test is specified as 0.36, while the intended x_f and a_f are assigned as 6.30 m and 9.60 cm, respectively. The comparisons of the free surface elevation at the focusing point and the impact forces on nets are given in Fig. 8. The results focus on the significant reciprocal interactions between the net panel and the focused wave occurring within 18.00 s and 22.00 s. The predominant evolutions of forces and free surface elevations are well captured through the numerical modelling. In combination with the time-series visualisations of wave fields over the net panel (see Fig. 9), the wave trough impacts the net panel firstly, resulting in the minima of occurring forces. Then the force magnitude rises in an instant as the interaction with the wave crest. The numerical simulation has captured the comparable features compared to the experiment, but the slight discrepancies in the phase and the amplitudes still exist. The relative errors of both amplitudes of forces and free surface elevations are 10.61% and 9.28%, respectively. The earlier wave focusing is driven by the practical unsteady interactions amongst wave components, the transfer of wave energies from lower to higher frequencies induces the reduction of the wave elevation at the theoretical focal point Tian et al. (2011). The overestimation of both amplitudes lies in the turbulence modelling error in the vicinity of free surfaces, as stated before. In short, the wave kinematics around the wave crest situations are not correctly represented. This statement also accounts for the differences as the wave crest passes over the panel. The current framework is unable to accurately model the processes of jet generation, jet falling and the subsequent backward flow toward the net panel, as observed experimentally in Fig. 9. A possible remedy for the current numerical method, such as incorporating large-eddy simulations in future solvers, is suggested based on the validation.

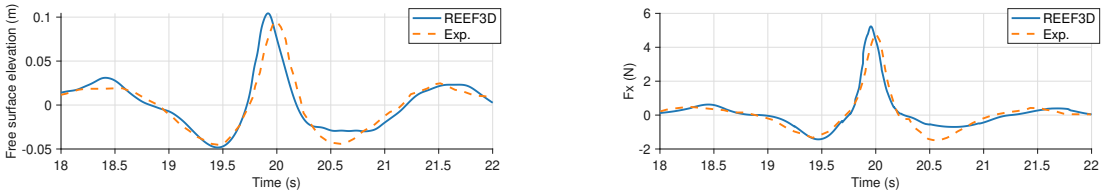

(a) Free surface elevation at the focusing point

(b) Wave impact forces on the net panel

Figure 8: Validation of the wave impact force on the net panel with $S_n = 0.23$.

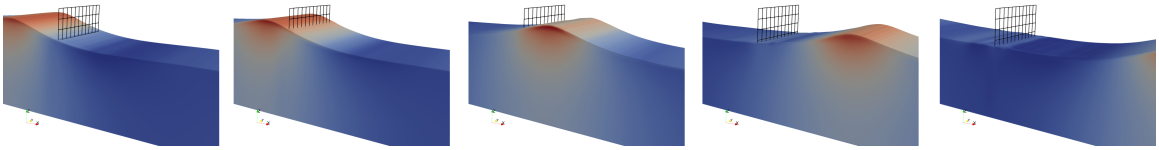

(a) REEF3D results

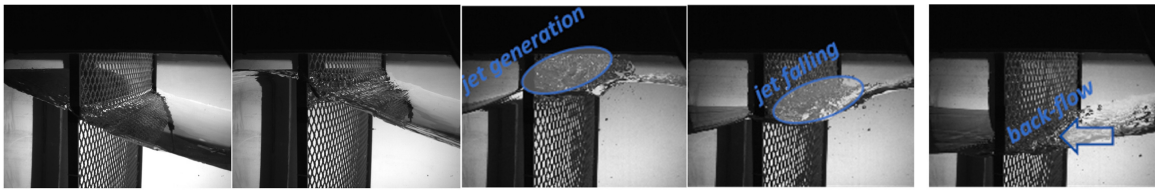

(b) Experimental observations

Figure 9: Comparisons of the time instances of wave crests over the net panel between the simulated and experimental observations, which is reprinted with the permission from Chen et al. (2024).

5 Results and discussions

5.1 Hydrodynamics of the PNAS in the focused breaking waves

It is well accepted that the dynamic responses of offshore structures can be more pronounced with the larger a_f in focused waves Zhu et al. (2023), and the dynamic response can be exacerbated by the placement factor. For example, the impact forces on the pile reach the maxima when the plunging breaker is curled down and impinges on the structure front without interacting with the free surface yet Tai et al. (2019). In this regard, a good hypothesis can thus be made that A9 with the placement of $x = 16.00$ m in Table 2 corresponds to the most exposed condition for the PNAS. It is adopted for further studies in section 5.1.1 and section 5.1.2, as the hydrodynamics of the net in focused waves deserve more discussions in this section.

5.1.1 Characteristics of impact forces on and wave fields around the PNAS

The characteristics of the wave impact loads and the non-linear wave-PNAS interactions during the evolution of the crest focusing and breaking are of considerable interest to the readers. The time-series of the non-dimensionalised horizontal impact forces on the PNAS within 37.00 s - 53.00 s at A9 are given in Fig. 10(a). In the early stage, it is presented that the horizontal force signals of piles and nets keep minor fluctuations around zero ahead of 42.50 s, which is attributed to the perturbation of the free surface in the pre-break situation (see Fig. 11(a)). It is followed by the gradually intensifying perturbation of the free surface prior to the ultimate focusing, leading to two secondary force peaks within 42.50 s - 44.00 s. The zero-crossing of the occurring horizontal forces in between roughly indicates the rapid transition of wave crest-to-trough situation, as proved in Fig. 11(a) and Fig. 11(b), relating to the reverse of the velocity vectors around the piles. Then at 44.88 s, the horizontal forces on both piles and nets escalate to the global peak simultaneously. The normalised magnitudes for

both structures reach 0.61 and 0.23, corresponding to 187.50 kN and 104.28 kN at prototype, respectively. Fig. 12 examines the interactions between the PNAS and the overturning breaker around the force peak moments of A9. Based on Fig. 11(b) and Fig. 12(a), it can be deduced that the wave crest experiences the processes of focusing and collapse over the duration from 44.00 s to 44.88 s. At 44.88 s, the overturning breaker initially strikes the pile and the net at a small contact area but with a significant velocity (see Fig. 12(b)), resulting in the global force peak in Fig. 10(a). Within the post-impingement phase for 44.88 s - 46.20 s, the horizontal force magnitudes drop to zero and the adverse force direction becomes distinct, which is the typical indicator of the developments of wave crest-to-trough scenarios (see Fig. 12(c), Fig. 12(d) and Fig. 11(c)). In addition to the blockage effects by the piles, the three-dimensional jet flow continues rolling, hitting the free surface and finally triggering the splash-up, which is consistent with the two-dimensional case. In accordance with the published work Yu et al. (2021), the prototype net renders more damping attempts on the focused wave futile, which is caused by the fairly low solidity of 0.15. This statement can be further enhanced quantitatively by a comparative case that the enclosed net is removed, as released in Fig. 10(a) and Fig. 10(b). The subjected horizontal forces of the piles in both pure-pile and PNAS cases stay aligned in terms of phases and amplitudes. From Fig. 11(d), the slight oscillation of the free surface elevation over an extended period following the impingement results in the oscillation of the horizontal forces in a similar manner with the pre-break instances, whereas it presents a more significant degree due to the impingement.

In order to gain better insights into the breaking wave impact effects on the structure, the wavelet spectra of the horizontal forces on the piles and net are provided in Fig. 10(c) and Fig. 10(d), respectively. The colour indicates the localised energy of the force magnitudes across time and frequency. The coexistence of high- and low-frequency harmonics at the impact moment has been confirmed intuitively, accompanied by a notable energy spiking event. The prominent peak keeps below 2.0 Hz, which is corresponding to the dominated frequency of the wave excitation. It must be emphasised that the piles are considered fixed in the present simulations, thereby the induced vibration or structural responses are not accounted for during the impact process. In other words, the aforementioned phenomenon of coexisting high- and low-frequency components should be primarily attributed to the transient impact effect generated when the breaking wave tongue strikes the pile surfaces and the net plane. Such a transient impact excites an extremely broad frequency range, with significant energy distribution over the spectrum Tai et al. (2019). Besides, the frequency bands excited by the wave impact are comparable for both structures, and the only difference lies in the amplitudes of energies. It suggests that the broad-frequency excitation is primarily driven by the transient characteristics of the impact itself, and the concentrated feature of energies is correlated with the structural differences to a limited extent.

Fig. 10(b) discussed the non-dimensional vertical forces on the PNAS. The varying slopes of the vertical components are more stable and the magnitudes are not behaving as violently as the occurring horizontal components. The normalised vertical force on the piles fluctuate over 0.11 - 0.16, while that of the nets merely reach up to 0.03. These are approximately one-fifth and one-eighth of the amplitudes of the horizontal wave forces, respectively. It further suggests that the water particle motion at the wave crest is predominantly horizontal with negligible vertical velocity, especially at the rolling breaker tongue, which can also be verified in the LES study of Cui et al. (2022).

Notwithstanding considerable variations in diameter between net twines and piles, the

impact forces on both manifest comparable time-evolution behaviours. The horizontal forces on the piles and nets are marginally out of phase, except for the situation when the breaker tongue strikes the structures. The plunging jet imposes an instantaneous impulse on the structure, so all contacting surfaces experience the surge at once. It is also confirmed from Fig. 10(c) and Fig. 10(d) that the broadband frequency excitations occur simultaneously. With respect to the onset of impingement by the breaker tongue, the horizontal force on the nets is 62.30% lower than that on the piles, but both are experiencing the surging of magnitudes in an instant. These findings have emphasised the susceptibility of net twines to stress-induced fracture under transient wave impacts, further exacerbated by the exclusion of the elastic modulus of net twines in the current study.

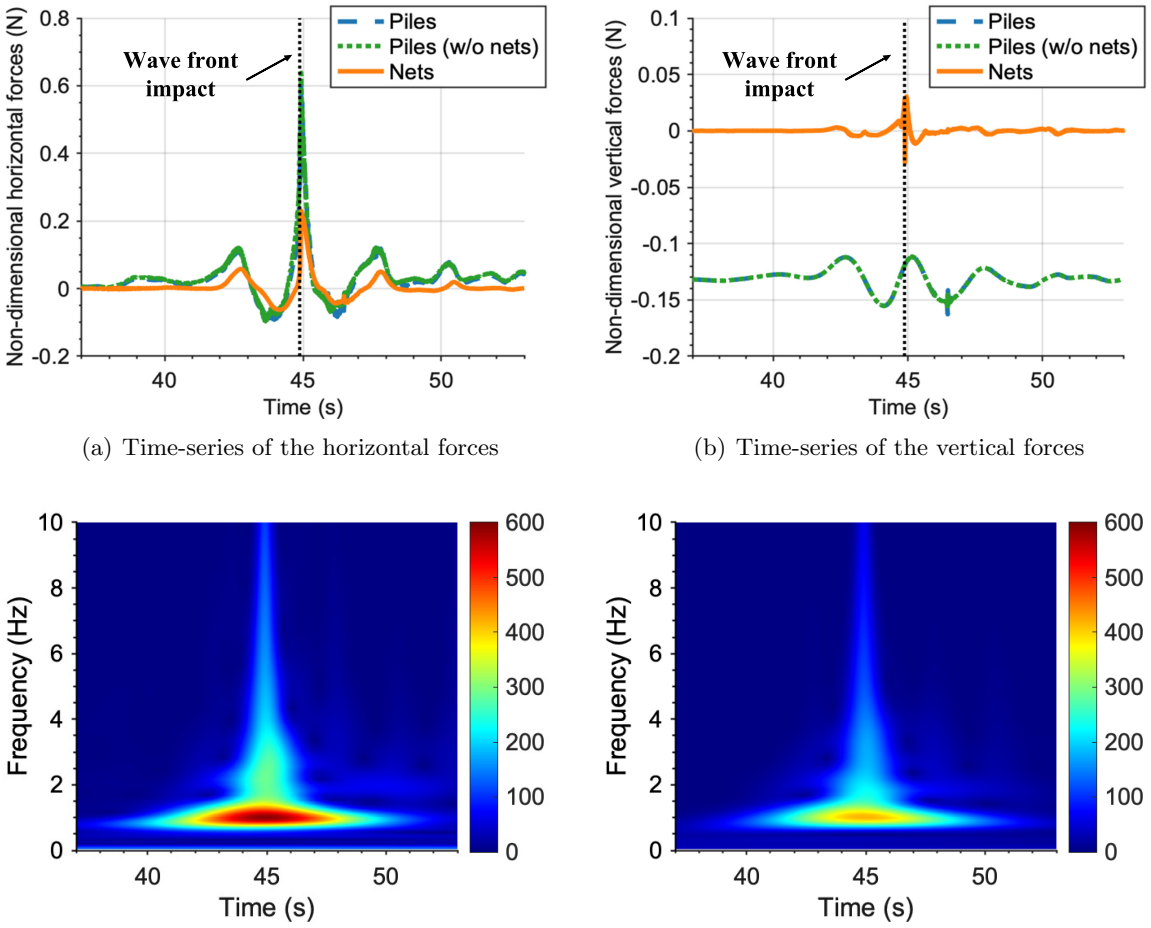

(a) Time-series of the horizontal forces

(b) Time-series of the vertical forces

(c) Wavelet spectra of the horizontal forces on the piles

(d) Wavelet spectra of the horizontal forces on the net

Figure 10: Time-series and wavelet spectra of the focused wave impact forces on the PNAS at A9. The dashed lines represent the moment when the wave front impacts the PNAS.

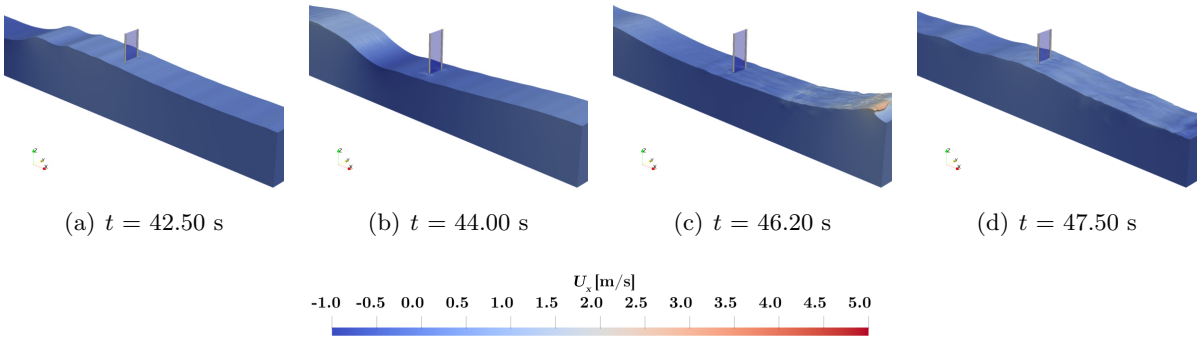

(a) $t = 42.50$ s (b) $t = 44.00$ s (c) $t = 46.20$ s (d) $t = 47.50$ s

Figure 11: Time instances of the interactions between the PNAS and the focused breaking wave at the prebreak and postbreak moments.

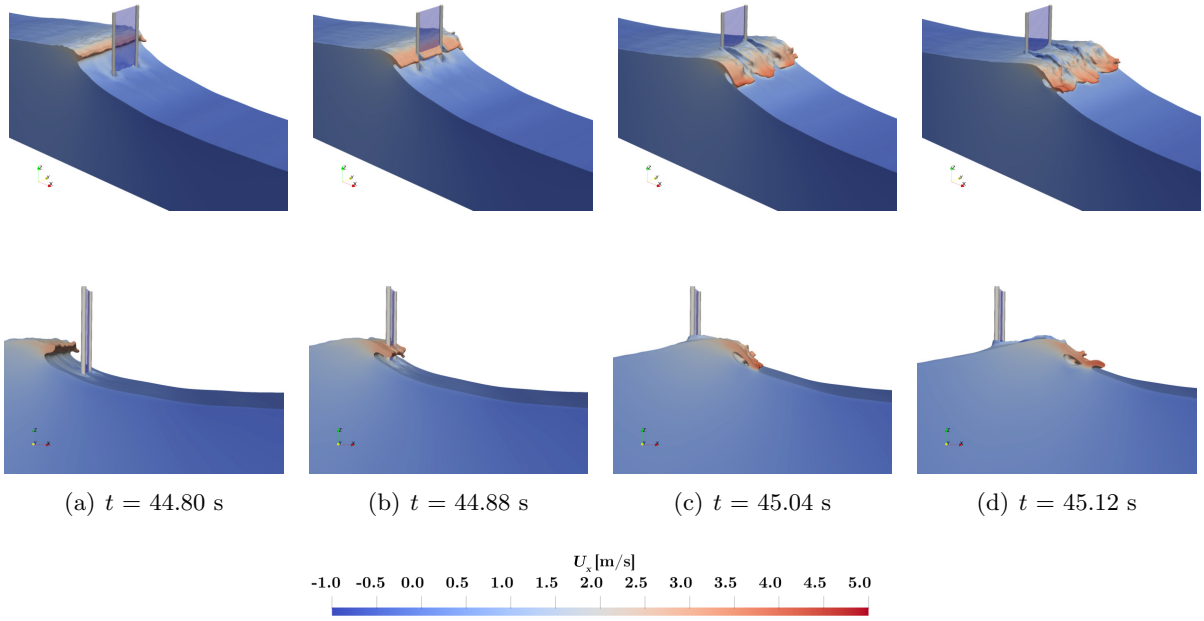

(a) $t = 44.80$ s (b) $t = 44.88$ s (c) $t = 45.04$ s (d) $t = 45.12$ s

Figure 12: Time instances of the interactions between the PNAS and the overturning breaker around the force peak moments of A9.

The local spanwise vorticity fields over the PNAS at $z = 0.8$ m around the wave focusing and breaking moments are given in Fig. 13, with allowance for a better understanding of the intense fluctuations of the occurring horizontal forces in between. Due to the reversed wave particle velocities, a pair of vortices develops and continuously separates from the pile surfaces, resulting in opposite-signed spanwise vorticity fields accompanied by a vortex shedding phenomenon in the negative x-direction. The onset of the breaker-impacting initialises the generation of the vortices in the positive x-axis instead, which is concerned with the transformation of the flow direction and can be verified at $t = 45.04$ s (Fig. 13(b)). After the

breaker impacts the free surface, the previously generated periodic vortex street remains in the negative x-direction, indicating that the flow direction transformation occurs quite rapidly. Fig. 13(c) presents the almost symmetrical-configured vortices with stable separations and shedding at $t = 45.28$ s, as a result of the dominated forward-directed flow. In short, the rapid evolutions of the vortices around the piles strongly support the intense fluctuations of the occurring horizontal forces on piles, and the shielding effects of the prototype net on the vortices' behaviours are negligible.

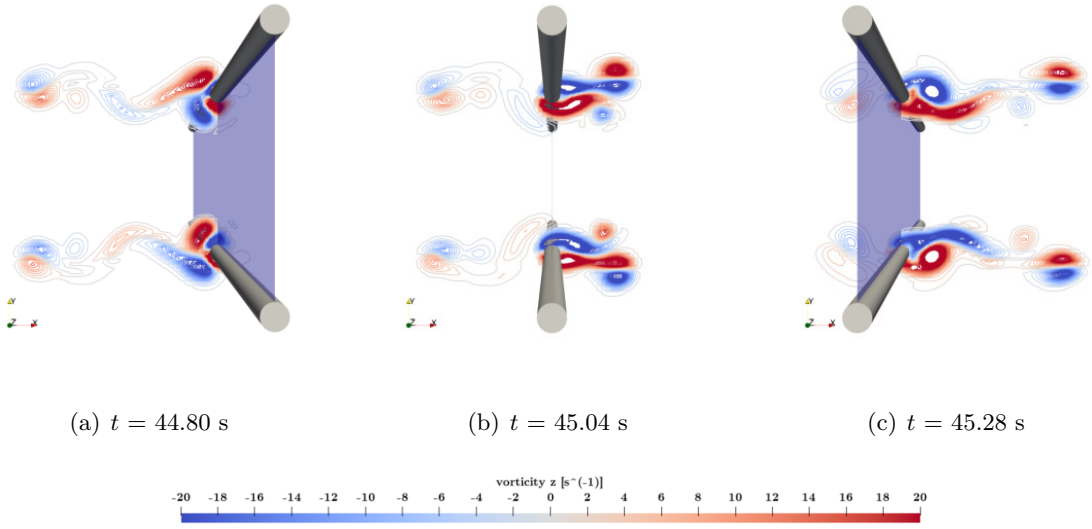

(a) $t = 44.80$ s (b) $t = 45.04$ s (c) $t = 45.28$ s

Figure 13: Distributions of the spanwise vorticity over the PNAS at z = 0.8 m around the wave focusing and breaking moments.

5.1.2 Distributions of local impact forces on the net

As addressed above, the occurring horizontal forces on the net account for a significant portion of the total forces on the whole structure, let alone the comparable features of the spectral distributions between the piles and the net. From a localised perspective, it is crucial to understand the impact forces concentrated in specific areas of the net before assessing the potential risks of net twine breakage. This section aims to address this need by presenting the local distribution patterns of the impact forces on the net, particularly at the moment the overturning breaker strikes the net plane.

Fig. 14 illustrates the spatial distribution of wave-induced impact forces on the net panel at the instant of peak wave-net interaction under a plunging breaker. As the plunging breaking wave tongue impinges on the panel, individual Lagrangian points of the net panel experience spatially varying impact forces. For the ease of visualisation, the net plane is spatially discretised into a uniform 20×20-grid pattern, with each macro screen denotes as 9.15 cm×1.85 cm. The impact forces from surrounding Lagrangian points are lumped to the nearest grid point based on geometric proximity, effectively mapping the continuous force field onto the discrete grid. Each grid is annotated with the resultant force magnitude in between, providing a spatially smoothed yet locally resolved depiction of the dynamic load distribution. The local peak value of the model-scale forces amongst all grids reaches 1.46 N - 1.52 N at the coordi-

nates (0.45 m, 1.35 m) and (0.55 m, 1.35 m), converting into an equivalent force magnitude of 3721 N - 3874 N in prototype. It should be noted that the peak force location coincides with the hotspot where the breaker tongue impacts the net panel vertically, causing the monotonic increase of the force magnitudes from 0.50 N to 1.50 N between the vertically adjacent grids. The breaker tongue, despite its slender geometry of only a few centimetres in thickness, is characterised by significant velocity and acceleration. Additionally, the force peaks generally arise at the lateral side of the piles horizontally and form a symmetrical pattern, particularly close to the central area. One potential reason for this observation is the cross-flow effects induced by the side-by-side circular piles, as supported by Kristiansen and Faltinsen (2012) and Wang et al. (2021), thus the local flow accelerations in the breaker layer can be expected.

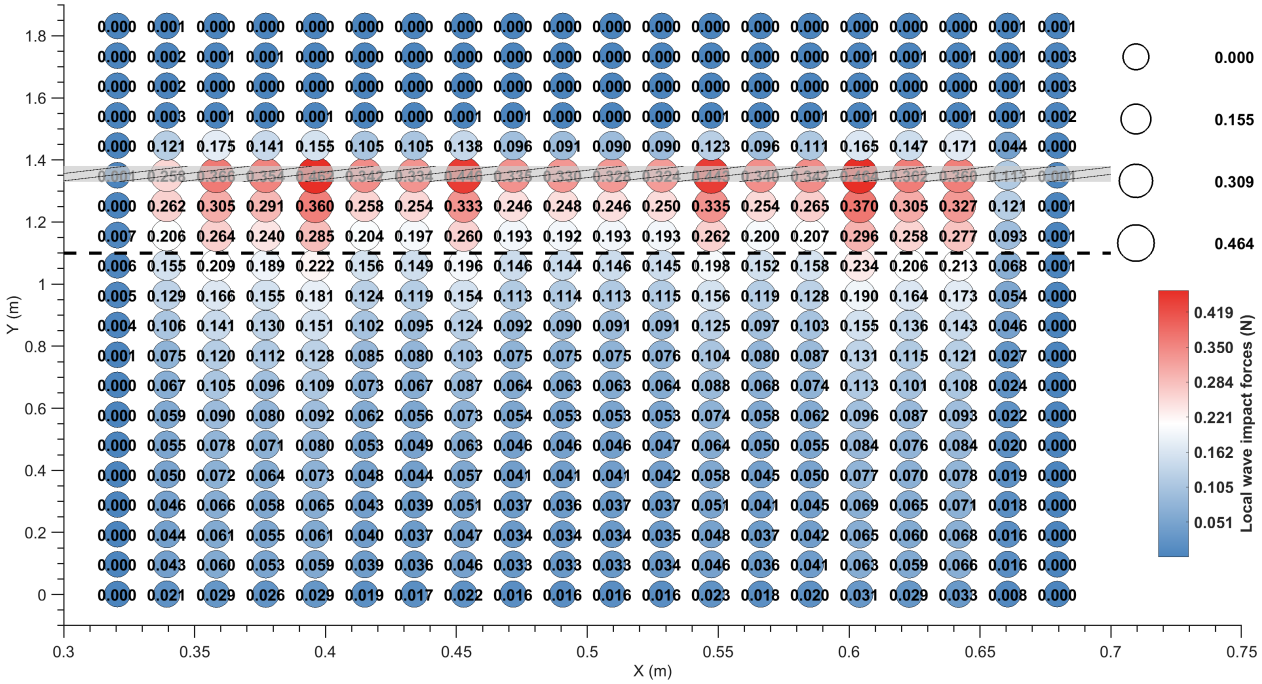

Figure 14: Distributions of the impact forces lumped at the 20×20 grids of the net panel. The dashed line indicates the SWL and the hatched zone in gray indicates the impact region by the breaker tongue.

5.1.3 Placement of the PNAS in the course of wave focusing and breaking

The intensity and the duration of the occurring wave forces are relevant to the placed locations of the PNAS, in which the wave front forms, focuses and breaks, creating the curled plunging breaker in the ultimate stages. In this study, the relationships between the different placed locations of the PNAS in the two-dimensional case of A9 are illustrated presumably in Fig. 15. The PNAS is oriented in the direction of wave propagation, allowing different stages to be experienced. In addition to the A9, B1 - B3 are established during the formation of the vertical wave front, which occurs ahead of the wave crest location. B4 corresponds to the situation that the secondary rolling jet owing to the initial splash-up observation strikes the PNAS, while B5 accounts for the PNAS in the context of the significant splash-up scenario.

The essential stages relating to the interactions between the PNAS and the focused breaking wave are all captured through the above cases.

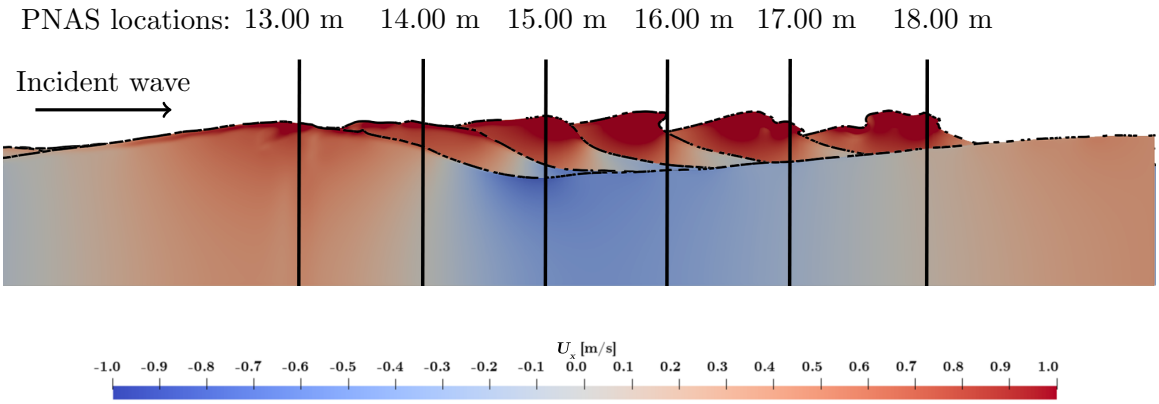

Figure 15: Schematic diagram of the different placements of the PNAS in the course of wave focusing and breaking.

As addressed before, the rapid surge of horizontal forces on the PNAS, particularly when the wave crest or breaker interacts with the structure, has emerged as a significant concern. This phenomenon poses potential threats, including unexpected net twine breakage or the exacerbation of the tearing processes of net panels. Table 3 lists the relevant data of the horizontal forces on the piles and nets at different placed locations with respect to the breaker. The total peak forces (TPF) on the PNAS, the dimensionless global peak forces ($\widetilde{\mathrm{GPF}}$) experienced by the piles and nets, the time of peak occurrence (TPO) as well as the local peak forces (LPF) on the net are included. It should be noted that a novel concept of the growth rate $\Delta N/\Delta t$ is introduced to characterise the initial surge in horizontal wave loads on the PNAS. It is defined as the ratio of the change in horizontal forces ΔN to a brief time interval Δt during which the wave front drives the horizontal force from a slight negative value to a sharp positive peak, thereby quantifying the rapidity of force escalation at impact. The standard deviation (STD) is also incorporated to assess the variability of the time-series horizontal forces.

The varying trend of TPF keeps the consistent with the $\widetilde{\mathrm{GPF}}$ and LPF of the piles and net with the advancement of the placed locations. These parameters rise monotonically until the interaction of the secondary rolling jet with the PNAS, then they are damped to the stable magnitudes as the energy embedded in the focused breaking wave is ultimately dissipated. The most pronounced case is A9 while the least one is B2. A striking difference is observed, with the LPF on the net in A9 exceeding that in B2 by a factor of 7.24. This statement hints at the correctness of the hypothesis at the beginning of this section and it is extended to net structures as well. Besides, the positive correlation between the growth rate and the peak forces is confirmed and the comparable observation is revealed in Kamath et al. (2016) as well. The growth rate approaches to the maxima even at case B3, which is close to the formation of the vertical wave front. The varying tendency of STDs is not as significant as peak values and growth rates across all cases, but it remains synchronised with the peak values.

Table 3: Statistical analysis of the horizontal forces on the piles and nets in the course of wave focusing and breaking. STD refers to the standard deviation of the time-series force data.

Cases	TPF [N]	Piles				Nets				
		$\widetilde{\text{GPF}}$ [-]	TPO [s]	$\Delta N/\Delta t$ [N/s]	STD	$\widetilde{\text{GPF}}$ [-]	TPO [s]	$\Delta N/\Delta t$ [N/s]	STD	LPF [N]
B1	59.00	0.32	43.98	40.95	8.22	0.13	44.06	32.13	5.81	0.22
B2	54.34	0.28	44.28	57.19	7.70	0.12	44.37	37.53	5.41	0.21
B3	79.46	0.45	44.54	87.06	7.98	0.16	44.6	54.83	5.61	0.50
A9	114.47	0.61	44.93	87.27	10.48	0.23	44.93	66.67	7.24	1.52
B4	96.26	0.49	45.29	56.45	9.32	0.22	45.3	57.14	6.78	1.34
B5	91.97	0.49	45.62	59.81	9.41	0.21	45.72	48.86	6.06	1.18

The least pronounced cases B1 and B2 relate to the early stage of wave focusing. Although there is a slight decrease in the $\widetilde{\text{GPF}}$ and LPF magnitudes in B2 compared to B1, B2 demonstrates a more significant growth rate. This is evidenced by the continuous accumulation of wave energy throughout the wave focusing process. Furthermore, it should be emphasised that the wave force characteristics of the PNAS in the post-breaking scenarios (B4 and B5) require more attention than the pre-breaking cases B1 - B3, particularly for nets, which can be corroborated by more considerable peak force values and STDs. This suggests that the impacting effects caused by the initial and the ultimate splash-up still outweigh the crest focusing process. A plausible explanation for this result is the rapid fluctuations and larger magnitudes in wave particle velocities that occur after wave breaking, which is supported through the comparisons of wave fields between case B3 and B4 around TPO in Fig. 16.

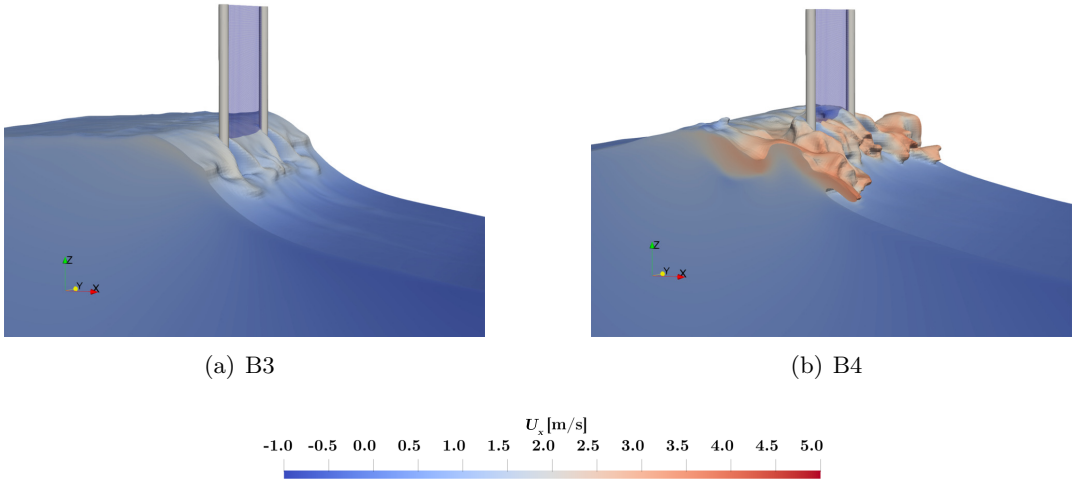

(a) B3 (b) B4

Figure 16: Time instances of the interactions between the PNAS and the focused breaking wave around TPO at case B3 and B4.

When comparing the wave force characteristics of the piles and the net, it is evident that the peak values, growth rates as well as STD for the net are generally less significant than those for the piles, with the exception of the growth rate observed in the case B4. But the TPO for both piles and nets are almost consistent within the band of 0.1 s, corresponding to the moment when the wave front impacts the structure. Given the prototypical net solidities

of 0.15, the distinction presumably arises from the significant porosity of the net panel, which is expected to be updated with the rising solidities due to bio-fouling issues.

Next, the wavelet spectra of the focused breaking wave impact forces on the piles and nets with different placed locations are provided in Fig. 17. The peak values of the wavelet power of the piles exhibit higher than that of the nets, showing an agreement with the results of peak force values, growth rates and STDs. The frequency relevant to the wavelet power peak in the spectra corresponds to the dominant wave excitation frequency, while its temporal occurrence coincides with the instant when the focused wave front impacts the PNAS structure. This observation holds true for both the pile and net components of the PNAS. A comparison of the time-frequency distributions of wavelet powers indicates similar patterns between B1 and B2, while another set of similarities is observed amongst B4, B5, and A9. These specific distribution characteristics are found to be governed by the different phases of focusing wave breaking development. A key observation is that with the placed position advances downstream from $x = 13.00$ m, the peak wavelet power values associated with the piles remain largely stable. On the contrary, a gradual attenuation of the peak wavelet power for the nets is recorded in the post-breaking stages. This finding suggests that the contrasting behaviour might primarily be attributed to the inherent differences in the structural features and responses of the pile and net systems. Moreover, the frequency band becomes broader with the advancement of the placed locations, with B1 and B2 oscillating around the dominant frequency of the incident wave, while B3 - B5 and A9 reach the upper frequency limit of 10 Hz. In the high-frequency region, the latter groups account for a larger fraction of the total wavelet power compared to the former. Additionally, the moderate high-frequency components (2 - 5 Hz) typically persist for 2 - 3 seconds, whereas the ultra-high-frequency components ($\sim$10 Hz) generally last for less than 1 second. This frequency distribution confirms again that post-breaking scenarios (B4 and B5) can be more challenging than pre-breaking cases, in terms of not only peak force, growth rate, and standard deviations, but also spectral characteristics.

5.2 Effects of focused amplitudes and peak frequencies on hydrodynamics of the PNAS

Given the constant placement $x = 16.00$ m of the PNAS, Table 4 reports the $\widetilde{\mathrm{GPF}}$, TPOs, growth rates and STDs of the horizontal impact forces experienced by the piles and nets with constant f_p while varying a_f, respectively. Increasing a_f leads to a monotonic decrease of the $\widetilde{\mathrm{GPF}}$ for both piles and net, rather than an increase. This behaviour follows directly from the adopted normalisation in Eq. 26. U_{wc} and H_w both grow approximately in proportion to a_f, so the denominator $\rho D H_w {U_{wc}}^2$ and $\rho G H_w S_n {U_{wc}}^2$ scales with ${a_f}^3$. For the fixed cylindrical structures in waves, the Morison force model decompose the total force into the inertia term F_I and drag term F_D, which are proportional to a_f and ${a_f}^2$, respectively. Therefore, $\widetilde{\mathrm{GPF}}$ can be roughly approximated as

$$\widetilde{\mathrm{GPF}} \approx \frac{F_I}{{a_f}^2} + \frac{F_D}{a_f}. \tag{31}$$

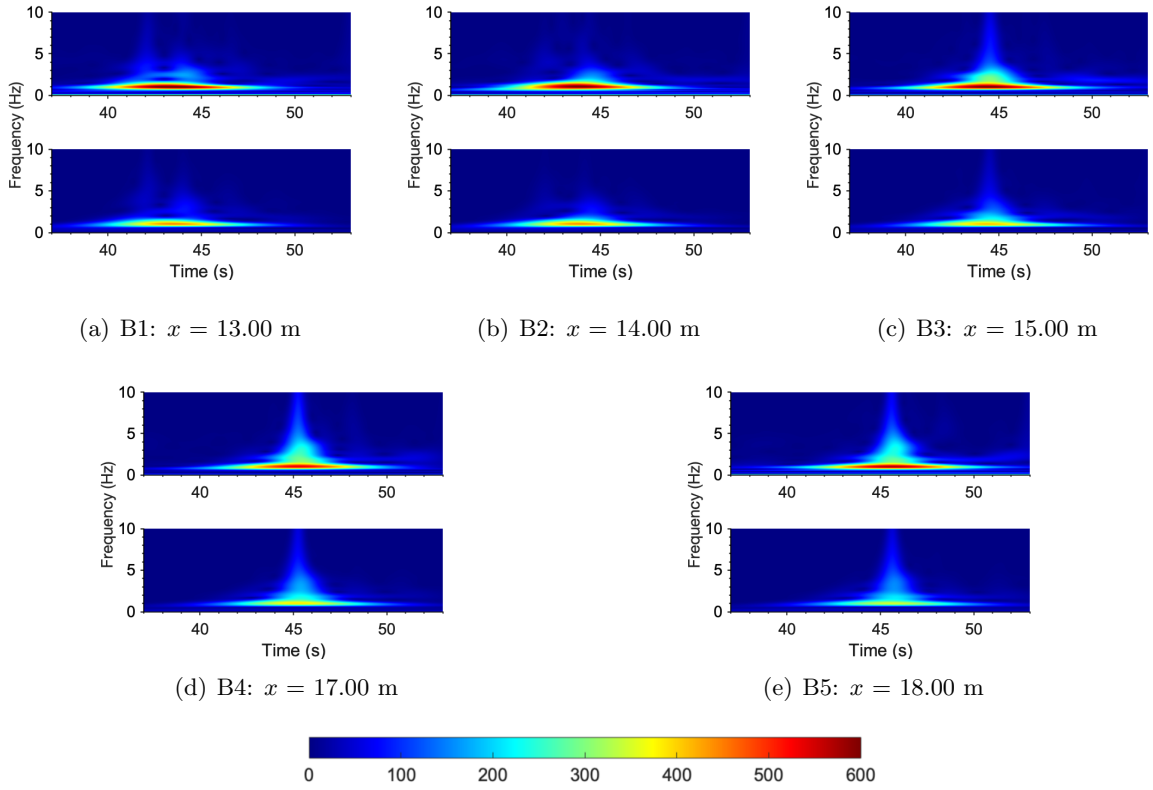

(a) B1: $x = 13.00$ m (b) B2: $x = 14.00$ m (c) B3: $x = 15.00$ m

(d) B4: $x = 17.00$ m (e) B5: $x = 18.00$ m

Figure 17: Wavelet spectra of the focused breaking wave impact forces on the piles and nets varying the placing locations. The upper subplot corresponds to the piles while the bottom one relates to the nets.

Table 4: Statistical analysis of the horizontal forces on the piles and nets with the increase of focused amplitudes. STD refers to the standard deviation of the time-series force data.

Cases	TPF [N]	Piles				Nets				
		$\widetilde{\mathrm{GPF}}$ [-]	TPO [s]	$\Delta N/\Delta t$ [N/s]	STD	$\widetilde{\mathrm{GPF}}$ [-]	TPO [s]	$\Delta N/\Delta t$ [N/s]	STD	LPF [N]
A1	5.95	9.99	45.25	4.21	1.15	3.14	45.50	2.74	0.50	0.02
A2	8.41	6.53	45.28	5.96	1.51	2.33	45.49	4.03	0.73	0.03
A3	11.36	4.59	45.29	8.39	1.97	1.81	45.47	5.67	1.06	0.06
A4	16.91	3.06	45.27	11.39	2.63	1.34	45.45	8.63	1.56	0.09
A8	107.80	0.62	45.12	57.40	9.96	0.27	45.13	61.81	7.55	0.80
A9	114.47	0.61	44.93	87.27	10.48	0.23	44.93	66.67	7.24	1.52

In the non-breaking regime and up to the onset of breaking, $\widetilde{\mathrm{GPF}}$ is proportional to the inverse ${a_f}^2$ for piles but this law is not applicable to nets. This implies that the global peak of piles occurs at a phase dominated by the inertial effect Esandi et al. (2020), while that of nets tends to be affected by the inertial and viscous drag effects simultaneously. Meanwhile, a mild upward trend in $\widetilde{\mathrm{GPF}} \cdot {a_f}^2$ for nets indicate an increasing drag share with a_f. This finding also aligns with the understanding that the viscous drag component contribute greater as the

Keulegan–Carpenter (KC) number increases Xu et al. (2021). By contrast, these relations cease to be linear and $\widetilde{\text{GPF}}$ tends to saturate as a_f grows in the breaking regime, because the slamming impulse and vigorous splash-up with significant dissipation of energy become overwhelmed and highly localised Cui et al. (2022).

Although the wave amplitude in A8 - A9 is only 2 - 3 times greater than that in A4, the indices including the growth rates and STD exhibit a much more substantial surging by a factor of 7.66 and 3.98, respectively. The non-linear correlations are highlighted here that the typical Morison force model or other empirical-based method cannot be utilised to estimate the resultant forces on the piles. A striking difference of 16.89 times in the LPF on the net (A9 versus A4) demonstrates the overwhelming effect of the breaking waves compared to the non-breaking ones, confirming the susceptibility of net twines to damage from the impact of the breaker tongue. Furthermore, it is also revealed that the $\widetilde{\text{GPF}}$, growth rates and STD of the net are not as significant as those of the piles, which has extended the previous finding in the breaking wave scenario to the non-breaking wave scenarios.

However, the out-of-phase phenomena occur for the TPO between the piles and net in the non-breaking wave cases, which can be reduced with the increase of a_f until the breaking stage. To address the distinction, a two-dimensional visualisation of the interactions between the free surface and the PNAS corresponding to two TPO at case A1 is presented in Fig. 18. It has been confirmed that the TPO for the net relates to the crest of the surface elevation, whereas that of the pile occurs prior to the crest forwarding. Thus, the TPOs for the piles are always ahead of that for the net. The velocity vectors of wave particles surrounding the net are perpendicular to it at the TPO, whereas the vectors around the piles are not. The observed difference further indicates that the loads acting on the piles are inertial-dominated Esandi et al. (2020), while the loads on the net depend more on drag forces due to the viscous effects.

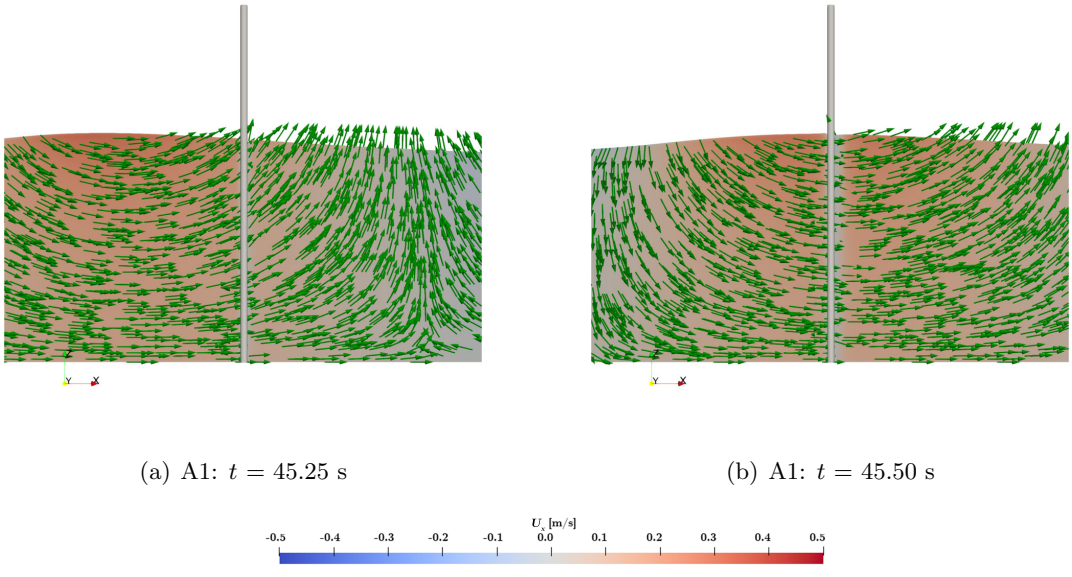

(a) A1: $t = 45.25$ s

(b) A1: $t = 45.50$ s

Figure 18: Interactions between the PNAS and the free surface on the X-Z Plane (2D View) at case A1. The green arrows indicate the directions of velocity vectors.

In this section, the focused wave cases with f_p = 0.35 Hz, 0.40 Hz, 0.45 Hz and 0.50 Hz correspond to A7, A3, A6 and A5, respectively. It can be seen from Table 5 that the $\widetilde{\text{GPF}}$ and STD of the horizontal impact forces on the piles and net present a declining trend with the rise of f_p, wherein the largest relative divergences amongst the relevant cases are 40.24% for the piles versus 53.71% for the net, respectively. Diverse from the LPF, the $\widetilde{\text{GPF}}$ of the net are more sensitive to f_p against the piles. A plausible explanation is that the change of f_p leads to the variation of the portion of the viscous drag components rather than the inertial components in the total wave loads, which can affect the occurring loads on the net more markedly than the piles Xu et al. (2021). Additionally, TPOs and the growth rates of the horizontal impact forces on the piles and net keep a steady oscillatory trend with f_p, within the relative error of 10 - 15% across this frequency domain. It has the implication that these parameters are not strongly sensitive to the change of frequencies in the non-breaking regime.

Table 5: Statistical analysis of the horizontal forces on the piles and nets with the increase of peak frequencies. STD refers to the standard deviation of the time-series force data.

Cases	TPF [N]	Piles				Nets				
		$\widetilde{\text{GPF}}$ [-]	TPO [s]	$\Delta N/\Delta t$ [N/s]	STD	$\widetilde{\text{GPF}}$ [-]	TPO [s]	$\Delta N/\Delta t$ [N/s]	STD	LPF [N]
A7	12.37	4.97	45.23	7.57	2.03	2.29	45.44	5.45	1.18	0.06
A3	11.36	4.59	45.29	8.39	1.97	1.81	45.47	5.67	1.06	0.06
A6	10.39	3.93	45.32	8.08	1.79	1.47	45.50	5.34	0.89	0.06
A5	9.42	2.97	45.35	7.93	1.69	1.06	45.53	5.38	0.77	0.06

Spectral analyses are carried out in Fig. 19 to reveal more information amongst the cases with varying a_f and f_p compared to the time-series responses. First, the frequency at the peak of the wavelet power coincides with the primary frequency of wave excitations. The peak values of the wavelet power of the piles are invariably larger than those of the nets, irrespective of the variations of a_f and f_p. Both findings align well with the comparisons in Section 5.1.3. As concerns the non-breaking wave cases with rising a_f (Fig. 19(a) - 19(b)), it is naturally found that the time-frequency patterns of wavelet powers are almost identical, except for the increase of wavelet energies. The onset of the breaking and plunging in A8 has expanded the frequency band to ∼10 Hz, and improved the peak of the wavelet energy by more than 3 times against A3. In short, the more severe the wave impact, the broader the frequency band covered by the excited force signal spectrum, ranging from low to high frequencies. In terms of the impacts by f_p, the time-frequency distributions amongst A7, A3 and A5 present in a similar manner, and there is no high frequency excitation within the non-breaking regime. Besides, the rise of f_p has shortened the time span of the marked wavelet powers of both piles and net, yet failed to affect the peak of the wavelet power, resulting in a rapid concentration of wave energy within a short time window, thereby imparting swift and significant loading on the structure. Consequently, a_f plays a crucial role in determining the frequency band and wavelet power intensities, while f_p primarily influences the duration of the marked wavelet powers.

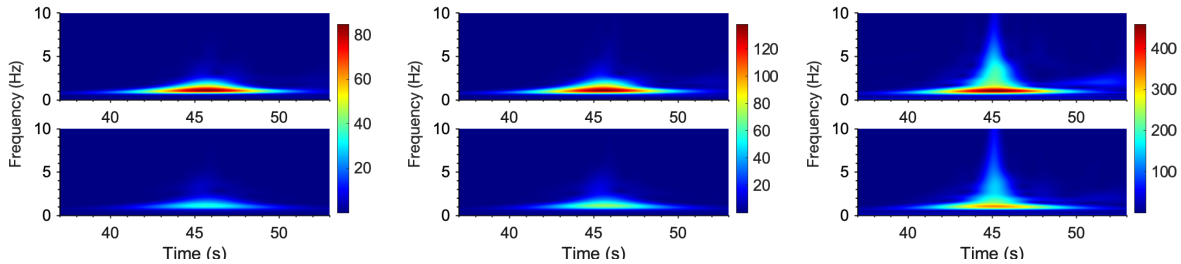

(a) A1: $a_f = 0.08$ m, $f_p = 0.40$ Hz (b) A3: $a_f = 0.12$ m, $f_p = 0.40$ Hz (c) A8: $a_f = 0.32$ m, $f_p = 0.40$ Hz

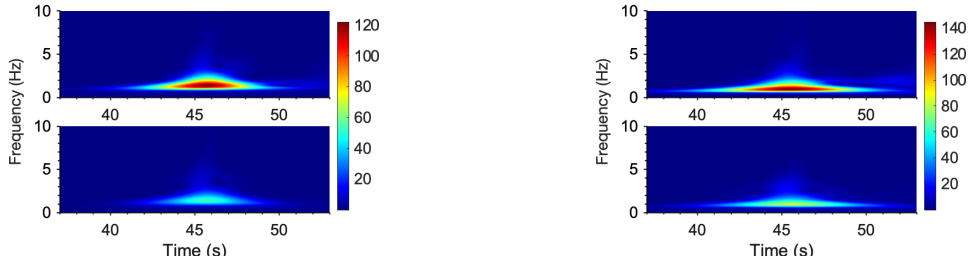

(d) A5: $a_f = 0.12$ m, $f_p = 0.50$ Hz (e) A7: $a_f = 0.12$ m, $f_p = 0.35$ Hz

Figure 19: Wavelet spectra of the focused breaking wave impact forces on the piles and nets varying the focused amplitudes and peak frequencies. The upper subplot corresponds to the piles while the bottom one relates to the nets.

5.3 Effects of net solidities on hydrodynamics of the PNAS in the focused breaking wave

The inevitable bio-fouling issues of nets within a prolonged service duration result in the rapid increase of net solidities, hence the occurring loads would spike dramatically even in regular wave scenarios Wang et al. (2022). This has the practical implication of evaluating the hydrodynamics of the PNAS subjected to the focused breaking wave loads, considering the extent of net solidities. Based on the preceding discussions concerning the wave loads, it is certified that the A9 with $x = 16.00$ m represents the most critical situation, which is thus utilised in this section.

Table 6 gives the peak forces, TPOs, the growth rates and the STDs of the horizontal impact forces experienced by the piles and nets with varying net solidities, respectively. First, it is found that the TPF on the PNAS, the $\widetilde{\text{GPF}}$ and the growth rates of the nets escalate invariably relative to the solidities. In contrast, the $\widetilde{\text{GPF}}$ of the piles presents a trend of an initial decrease followed by a linear increase pattern, as the net solidities rising from 0.1 to 0.5. This varying tendency diverges significantly from our published works Wang et al. (2022), which states that the horizontal forces on the frames of offshore fish farms are independent of net solidities. The incident wave types can account for the differences, wherein the focusing breaking wave exhibits significant net water transport as the plunging jet propels water forward during breaking, followed by intense post-breaking turbulence, whereas in a second-order Stokes wave, water particles primarily undergo oscillatory motion with negligible

net displacement, returning nearly to their original positions after each cycle. The mutual flow interaction between the side-by-side piles and the net is another clarification for the difference. As shown in Fig. 20, the focused breaking wave inherently creates pressure differences on the suction and pressure sides of the net. The induced pressure jump over the net in case A9 is not as significant as that in case C5, allowing most of the incident wave-induced flow to pass through. But this pattern gets reversed with its influence extending to the piles, which can be more evident in the case of $S_n = 0.5$. The fluctuations of pressure fields around piles and nets lead to the non-monotonic evolution of $\widetilde{\text{GPF}}$ of piles with solidities. This finding highlights the unique flow–flow interactions under extreme waves, indicating that the findings from previous studies on individual piles or nets alone are not directly applicable to the PNAS. Further, the TPOs are unaffected by the net solidities, and the STDs follow the varying laws of the peak values in a similar manner.

Table 6: Statistical analysis of the horizontal forces on the piles and nets relating to net solidities. STD refers to the standard deviation of the time-series force data.

Cases	TPF [N]	Piles				Nets				
		$\widetilde{\text{GPF}}$ [-]	TPO [s]	$\Delta N/\Delta t$ [N/s]	STD	$\widetilde{\text{GPF}}$ [-]	TPO [s]	$\Delta N/\Delta t$ [N/s]	STD	LPF [N]
C1	100.89	0.61	44.94	66.04	10.34	0.23	44.95	45.74	4.58	0.94
C2	140.67	0.60	44.94	86.55	9.93	0.28	44.94	101.71	10.64	2.40
C3	213.23	0.66	44.93	100.21	11.14	0.37	44.94	193.52	20.88	4.20
C4	312.00	0.70	44.93	118.22	11.58	0.47	44.94	350.88	34.92	6.45
C5	445.32	0.75	44.92	134.27	12.56	0.59	44.93	554.30	58.25	8.42

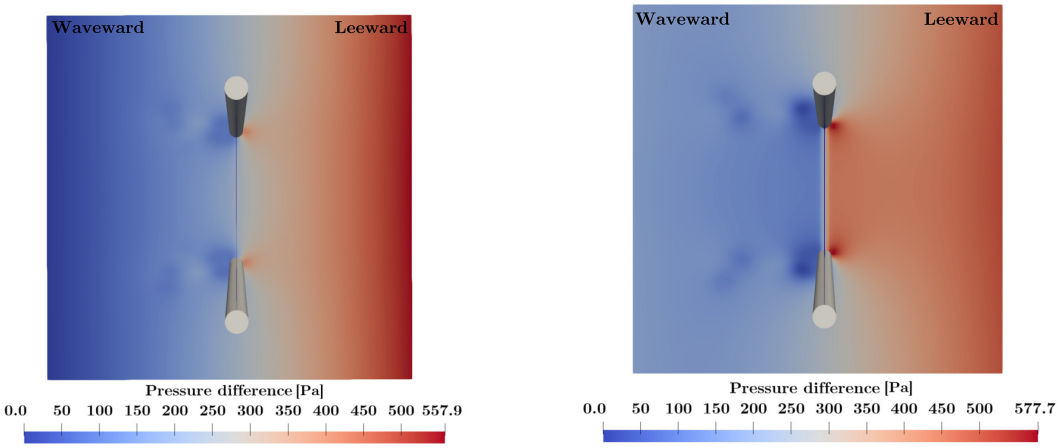

(a) A9 (b) C5

Figure 20: Distributions of the pressure fields around the PNAS in cases A9 and C5.

One can recall that the LPF on the prototype net with the $S_n = 0.15$ achieve 1.52 N, equalling 3874.32 N through the full-scale conversion. What is remarkable is that the LPF reaches 8.42 N (21461.70 N in prototype) at $S_n = 0.50$, which is 5.54 times larger than the prototype net without the bio-fouling effects and farther beyond the tensile stiffness of the

PET material. This underscores the critical importance of prompt and effective bio-fouling clearance on net systems of offshore aquaculture structures ahead of extreme storm surges.

The TPF on the PNAS, the $\widetilde{\mathrm{GPF}}$ as well as LPF on the net can be presented by the polynomial curve fit as the functions of S_n, in order to include more severe bio-fouling situations under the impact of the focused breaking wave for further predictions. Based on the existing data, the second-order polynomial fitting is applied for describing the nonlinear relationship, which is given as

$$\begin{aligned}
\mathrm{TPF} &= 1520.09{S_n}^2 - 49.00S_n + 89.53, \mathcal{R}^2 = 99.99\%, \\
\widetilde{\mathrm{GPF}} &= 1.03{S_n}^2 + 0.32S_n + 0.18, \mathcal{R}^2 = 99.65\%, \\
\mathrm{LPF} &= 10.33{S_n}^2 + 12.96S_n - 0.56, \mathcal{R}^2 = 99.86\%.
\end{aligned} \tag{32}$$

The proposed empirical formulae demonstrate the excellent performance, with the goodness of fit $\mathcal{R}^2$ exceeding 0.99. The relationship between those indices and solidities further supports the hydrodynamics results of the field samplings of the hydroid-fouled nets in Bi et al. (2018). Nonetheless, the applicability of Eq. (32) considering other parametrial variations of focused waves and structures deserve more validations and refinements.

Fig. 21 displays the wavelet spectra of the impact forces on the piles and net for case C5. When compared to the spectrum in case A9 (see Fig. 10(c) and 10(d)), it is evident that the peak and the extent of the induced wavelet energy for the net have significantly increased, while those for the piles show only marginal changes. These findings further support the direct relationship between wavelet power and the peak values of wave loads in cases with varying values of S_n. In previous sections of this study, the time-frequency distribution patterns were explained in relation to the structural characteristics and placements of the PNAS. However, it is important to note that the time-frequency distributions of wavelet powers in case C5 remain consistent with those in case A9. Essentially, the method used to represent the critical bio-fouling feature in the numerical analysis involves increasing net solidities isotropically, which minimises discrepancies in the time-frequency distribution properties. It should be emphasised that this approach does not fully align with the actual characteristics of biofouled nets, which host various types of fouling Chen et al. (2023) and lead to structural differences to some extent. Therefore, further experimental measurements are essential to verify the spectral results for nets in future studies.

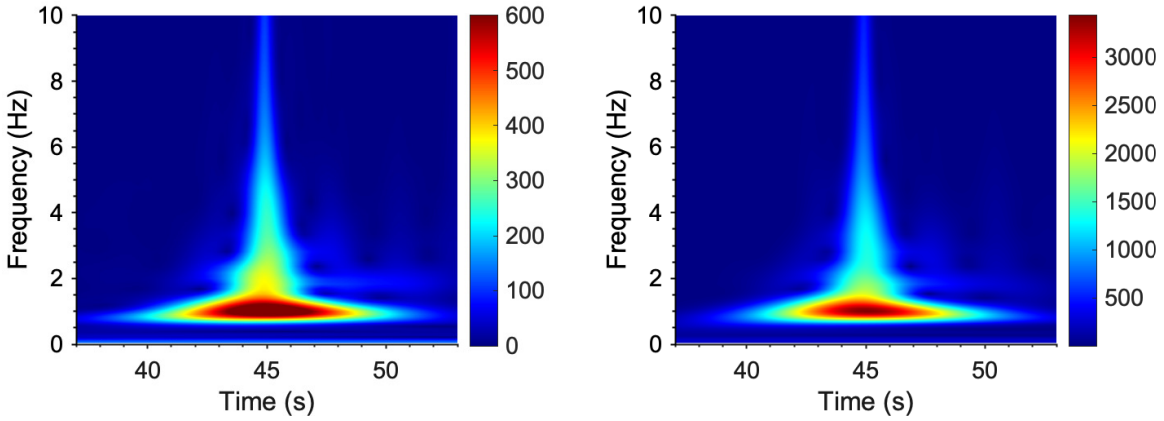

(a) Piles (b) Net

Figure 21: Wavelet spectra of the impact forces on the PNAS at case C5.

6 Conclusions

In this paper, a numerical study of modelling the interactions between the pile-net aquaculture structures (PNAS) and the focused waves is presented using the open-source hydrodynamics toolbox REEF3D. The utilised framework is composed of a high-fidelity computational fluid dynamics (CFD)-based numerical wave tank (NWT), wherein the NewWave theory and the Pierson-Moskowitz (PM) spectrum account for the generation of the focused waves. The disturbance of viscous fluids by rigid bodies and nets is incorporated via two additional forcing terms, formulated with a direct forcing immersed boundary method (DF-IBM) and a Lagrangian–Eulerian coupling algorithm, respectively. An enhanced continuous treatment for the densities between solid and fluid phases has improved the robustness and efficiency for modelling the rigid bodies in extreme waves.

The accuracies of the NWT and the impact forces are initially verified and validated. In relation to the most exposed environmental condition, the hydrodynamic characteristics of the PNAS, including the impact forces, surrounding wave fields as well as the distributions of the local impact forces on nets, are discussed in the time and frequency domains. Further, the impacts of placements of the PNAS, wave parameters as well as net solidities on the impact forces and wave fields, are investigated in detail. The main conclusions are summarised as follows:

- At the moment when the plunging breaker strikes the pile and the net, the impact forces on both structures escalate to the global peak simultaneously. The normalised peaks for both reach 0.61 and 0.23, corresponding to 187.50 kN and 104.28 kN, respectively. The wavelet spectra of impact forces have confirmed the coexistence of high- and low-frequency harmonics in the horizontal forces with the excitation of the plunger, as well as the pronounced wavelet energy spiking.

- It is revealed that the local impact forces on the net can reach 3721 N - 3874 N in prototype. The local peak force location coincides with the hotspot where the breaker

tongue impacts the net panel vertically. The susceptibility of net twines to stress-induced fracture under transient wave impacts has been addressed in this study.

- Placing the PNAS closer to the point of wave breaking significantly increases the peak forces and their variability relative to positioning it earlier in the wave focusing process. However, the violent splash-up events in the post-breaking stage impart greater loads on the PNAS than even the crest focusing stage of the wave, due to the rapid fluctuations and larger magnitudes in wave particle velocities that occur after wave breaking.

- The rise of focused amplitudes and peak frequencies leads to the monotonic decrease of the dimensionless peak forces on the PNAS. In the non-breaking regime, the loads on piles are dominated by inertial effects, while that on nets are more affected by viscous drag effects. In the breaking regime, the dimensionless peak forces on the PNAS tend to saturate with the rise of focused amplitudes, because the slamming impulse and vigorous splash-up become overwhelmed and highly localised.

- The unique flow–flow interactions around piles and nets are addressed when the net solidity reaches 0.5. The second-order polynomial formulae to predict the total peak forces on the PNAS, the dimensionless peak forces as well as the local peak forces on the net are proposed as the functions of net solidities.

The present study examines the non-linear responses of the PNAS concerning the impact of extreme waves. This research enhances the existing knowledge base and updates guidelines for structural design and optimization. However, certain limitations should be addressed in future work, particularly by modelling the structural responses of piles and nets. For example, the phenomenon known as "ringing" which occurs in piles after the impact of breaker jets, oscillates at approximately its natural frequency and is induced by elasticity. This aspect should be evaluated in future studies. Additionally, the ongoing development of the mutual FSI scheme contributes to the understanding of the hydroelasticity of flexible nets as focused waves progress.

A Continuous density treatment

In the previous FSI solver Martin et al. (2021); Wang et al. (2022), the application of level set methods for phase delineation between rigid-body and fluid domains introduces numerical instabilities, primarily stemming from rapid variations in gradient fields at interfacial regions. To address this issue, the default thickness of the transition layer $\epsilon = 2.1\Delta x$ is utilised to capture the considerable variations of densities. The discontinuous density methodology demands a huge amount of computational resources but also results in the spurious pressure fields in the near-field regions (Fig. 22(a)). Besides, the forcing term would also spike as the significant hydrodynamics interactions for rigid bodies in extreme waves, even if rendering more refined computational grids futile as well.

As depicted in Fig. 22(b), an enhanced continuous treatment for densities is incorporated. Eq. (3) is enabled inside rigid bodies while Eq. (14) still holds its validity to enclose the fluid-structure coupling. It rather hints at the possibility of using a thinner transition layer between solid and fluid phases, thereby the material properties of air and water can be smeared out

smoothly. The drastic variations in density gradients and spurious pressure fields and tangential velocities near boundaries are prevented. Thus, the deployment of coarser computational grids around rigid bodies without sacrificing accuracy makes it computationally more efficient.

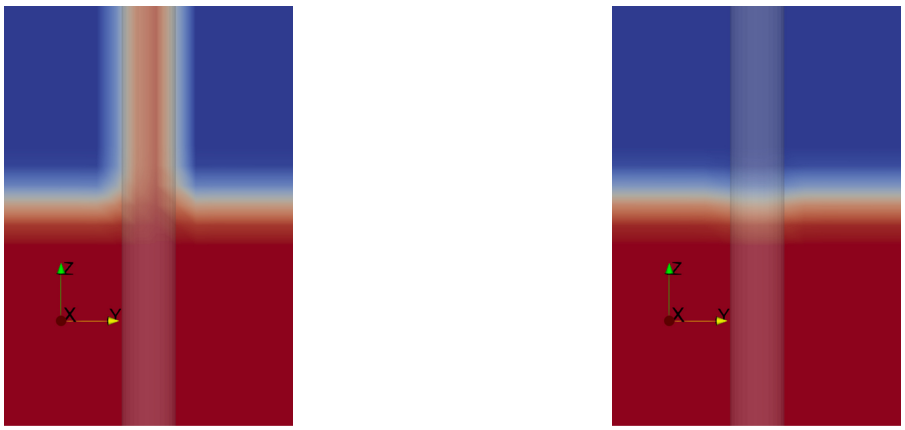

(a) Discontinuous density methodology (b) Continuous density methodology

Figure 22: Sketch of the density treatments. The rigid body has been processed transparently for visualisation.

Acknowledgment

This work was financially supported by Shandong Key R&D Program (Competitive Innovation Platform) (2024CXPT071-3); National Natural Science Foundation of China (No. 32303072, 52501335); Shandong Provincial Natural Science Foundation (No. ZR2023QC005); Central Public-interest Scientific Institution Basal Research Fund, CAFS (20603022024021, BRESG-JB202518); Young Elite Scientists Sponsorship Program by CAST (No. 2023QNRC001). The authors acknowledge Dr. Guixun Zhu (National University of Singapore) and Dr. Qiupan Chen (China Power Engineering Consulting Group Co., Ltd.) for their guidance on wave hydrodynamics in this paper.

CRediT authorship contribution statement

Gang Wang: Conceptualisation, Formal analysis, Funding acquisition, Writing - Original draft, Writing - Review & Editing. **Ting Cui:** Investigation, Visualisation, Writing - Review & Editing. **Bing Tai:** Conceptualisation, Data Curation, Methodology, Writing - Review & Editing. **Changtao Guan:** Supervision, Project administration, Funding acquisition. **Ahmet Soydan:** Methodology, Writing - Review & Editing. **Widar Weizhi Wang:** Methodology, Writing - Review & Editing. **Hans Bihs:** Conceptualisation, Methodology, Writing - Review & Editing, Supervision.

Declaration of competing interest

The authors declare that they have no known competing financial interests or personal relationships that could have appeared to influence the work reported in this paper.

References

Y. Chu, C. Wang, J. Park, P. Lader, Review of cage and containment tank designs for offshore fish farming, Aquaculture 519 (2020) 734928.

S. Wang, D. Feng, F. Gui, Z. Xu, Dynamic behavior of the net of a pile–net-gapped enclosure aquaculture facility, Journal of Marine Science and Engineering 10 (2022) 1166.

Y.-I. Chu, C.-M. Wang, H. Zhang, N. Abdussamie, H. Karampour, D.-S. Jeng, J. Baumeister, P. A. Aland, Offshore fish farms: a review of standards and guidelines for design and analysis, Journal of Marine Science and Engineering 11 (2023) 762.

Z. Wang, G. Wang, Z. Jiao, D. Feng, X. Qu, F. Gui, Hydrodynamics of PET net panels using the improved delayed detached eddy simulation (in Chinese with English abstract), Journal of Fisheries of China 48 (2024) 129610.

Z.-Q. Fan, Y.-H. Liang, Z. Yun-Peng, Review of the research on the hydrodynamics of fishing cage nets, Ocean Engineering 276 (2023) 114192.

S. Tavakoli, M. Singh, S. Hosseinzadeh, Z. Hu, Y. Shao, S. Wang, L. Huang, A. Grammatikopoulos, Y. P. Li, D. Khojasteh, J. Liu, A. Dolatshah, H. Cheng, S. Hirdaris, A review of flexible fluid-structure interactions in the ocean: Progress, challenges, and future directions, Ocean Engineering 342 (2025) 122545.

K. Wang, Y. Yang, G. Reniers, Q. Huang, A study into the spatiotemporal distribution of typhoon storm surge disasters in China, Natural Hazards 108 (2021) 1237–1256.

C. Kharif, Rogue waves in the ocean, Advances in geophysical and environmental mechanics and mathematics ser, Springer Berlin / Heidelberg, Berlin, Heidelberg, 2009.

M. L. McAllister, S. Draycott, R. Calvert, T. Davey, F. Dias, T. S. Van Den Bremer, Three-dimensional wave breaking, Nature 633 (2024) 601–607.

C. Mi, J. Gao, Z. Song, Y. Liu, Hydrodynamic wave forces on two side-by-side barges subjected to nonlinear focused wave groups, Ocean Engineering 317 (2025) 120056.

J. Gao, X. Ma, J. Zang, G. Dong, X. Ma, Y. Zhu, L. Zhou, Numerical investigation of harbor oscillations induced by focused transient wave groups, Coastal Engineering 158 (2020) 103670.

S. Normannsen, Measuring the impact of extreme waves on offshore structures, https://norwegianscitechnews.com/2021/08/measuring-the-impact-of-extreme-waves-on-offshore-structures/, 2021. 2025-10-13.

H. Yang, Z. Xu, C. Bi, Y.-P. Zhao, Numerical modeling of interaction between steady flow and pile-net structures using a one-way coupling model, Ocean Engineering 254 (2022) 111362.

H. Wang, X. Zhang, X. Zhang, X. Li, X. Tian, Y. Shen, W. Song, Experimental investigations on hydrodynamic interactions between the cylinder and nets of a typical offshore aquacultural structure in steady current, Marine Structures 88 (2023) 103367.

C. Chen, H. Wang, X. Zhang, X. Zhang, Hydrodynamic interactions between the cylinder and nets of a typical offshore aquaculture structure in steady current: Numerical investigation and coupling mechanism, Marine Structures 97 (2024) 103657.

Y.-P. Zhao, L.-X. Xin, C. Ma, K.-Z. Fang, Y.-X. Li, C.-W. Bi, Numerical study on wave propagating characteristics through an offshore pile-net enclosure structure, Ocean Engineering 314 (2024) 119801.

W. Xie, Z. Jiang, Y. Zheng, Z. Liang, A study of the vibration properties of a pile-net structure under wave-induced excitations, Biosystems Engineering 254 (2025) 104139.

G. Wang, Z. Jiao, C. Guan, A. Soydan, W. W. Wang, H. Bihs, Modelling focused breaking wave interactions with pile-net aquaculture structures (PNAS) using REEF3D, in: Proceedings of the ASME 2025 44th International Conference on Ocean, Offshore and Arctic Engineering, volume Volume 2: Subsea Technology; Ocean Space Utilization, ASME, Vancouver, British Columbia, Canada, 2025, p. V002T05A005. V002T05A005.

B. Tai, Y. Ma, G. Dong, Experimental study on plunging breaking waves impacting a vertical cylinder with three different model scales, Ocean Engineering 312 (2024) 119347.

T.-J. Xu, G.-H. Dong, M.-F. Tang, J. Liu, W.-J. Guo, Experimental analysis of hydrodynamic forces on net panel in extreme waves, Applied Ocean Research 107 (2021) 102495.

Q.-P. Chen, C. Ma, Y.-P. Zhao, C.-W. Bi, H.-F. Liu, Hydrodynamics of focused waves acting on netting that extends above the mean sea level, Ocean Engineering 309 (2024) 118516.

J. Gao, C. Mi, Z. Song, Y. Liu, Transient gap resonance between two closely-spaced boxes triggered by nonlinear focused wave groups, Ocean Engineering 305 (2024) 117938.

C.-l. Mi, J.-l. Gao, Z.-w. Song, M.-y. Yan, Gap resonance between a stationary box and a vertical wall induced by transient focused wave groups, China Ocean Engineering 39 (2025) 441–454.

J. Gao, Y. Wu, Z. Song, M. He, Influences of low velocity uniform current on characteristics of gap resonance occurring between two adjacent fixed bodies, Marine Structures 106 (2026) 103961.

P. S. Tromans, A. R. Anaturk, P. Hagemeijer, A new model for the kinematics of large ocean waves-application as a design wave, in: The First International Offshore and Polar Engineering Conference, 1991, pp. ISOPE–I–91–154.

DC. Wilcox, Turbulence modeling for CFD, DCW industries, La Canada (1998).

P. A. Durbin, Limiters and wall treatments in applied turbulence modeling, Fluid Dynamics Research 41 (2009) 012203.

H. Bihs, A. Kamath, M. Alagan Chella, A. Aggarwal, Ø. A. Arntsen, A new level set numerical wave tank with improved density interpolation for complex wave hydrodynamics, Computers & Fluids 140 (2016) 191–208.

S. Osher, J. A. Sethian, Fronts propagating with curvature-dependent speed: algorithms based on Hamilton-Jacobi formulations, Journal of Computational Physics 79 (1988) 12–49.

M. Sussman, P. Smereka, S. Osher, A level set approach for computing solutions to incompressible two-phase flow, Journal of Computational Physics 114 (1994) 146–159.

D. Peng, B. Merriman, S. Osher, H. Zhao, M. Kang, A PDE-based fast local level set method, Journal of Computational Physics 155 (1999) 410–438.

G.-S. Jiang, C.-W. Shu, Efficient implementation of weighted ENO schemes, Journal of Computational Physics 126 (1996) 202–228.

G.-S. Jiang, D. Peng, Weighted ENO schemes for Hamilton–Jacobi equations, SIAM Journal on Scientific Computing 21 (2000) 2126–2143.

P. R. Spalart, R. D. Moser, M. M. Rogers, Spectral methods for the Navier-Stokes equations with one infinite and two periodic directions, Journal of Computational Physics 96 (1991) 297–324.

L. J. P. Timmermans, P. D. Minev, F. N. Van De Vosse, An approximate projection scheme for incompressible flow using spectral elements, International Journal for Numerical Methods in Fluids 22 (1996) 673–688.

H. A. Van Der Vorst, Bi-CGSTAB: A fast and smoothly converging variant of Bi-CG for the solution of nonsymmetric linear systems, SIAM Journal on Scientific and Statistical Computing 13 (1992) 631–644.

M. Longuet-Higgins, Breaking waves in deep or shallow water, in: Proc. 10th Conf. on Naval Hydrodynamics, volume 597, MIT, 1974, p. 605.

W. Wang, C. Pákozdi, A. Kamath, H. Bihs, A fully nonlinear potential flow wave modelling procedure for simulations of offshore sea states with various wave breaking scenarios, Applied Ocean Research 117 (2021) 102898.

W. J. Pierson, L. Moskowitz, A proposed spectral form for fully developed wind seas based on the similarity theory of s. a. kitaigorodskii, Journal of Geophysical Research 69 (1964) 5181–5190.

H. A. Schäffer, Second-order wavemaker theory for irregular waves, Ocean Engineering 23 (1996) 47–88.

D. Ning, J. Zang, S. Liu, R. Eatock Taylor, B. Teng, P. Taylor, Free-surface evolution and wave kinematics for nonlinear uni-directional focused wave groups, Ocean Engineering 36 (2009) 1226–1243.

H. Bihs, A. Kamath, A combined level set/ghost cell immersed boundary representation for floating body simulations, International Journal for Numerical Methods in Fluids 83 (2017) 905–916.

L. Yang, One-fluid formulation for fluid–structure interaction with free surface, Computer Methods in Applied Mechanics and Engineering 332 (2018) 102–135.

T. Martin, A. Tsarau, H. Bihs, A numerical framework for modelling the dynamics of open ocean aquaculture structures in viscous fluids, Applied Ocean Research 106 (2021) 102410.

T. Kristiansen, O. M. Faltinsen, Modelling of current loads on aquaculture net cages, Journal of Fluids and Structures 34 (2012) 218–235.

T. Martin, A. Kamath, H. Bihs, A Lagrangian approach for the coupled simulation of fixed net structures in a Eulerian fluid model, Journal of Fluids and Structures 94 (2020) 102962.

C. S. Peskin, Numerical analysis of blood flow in the heart, Journal of Computational Physics 25 (1977) 220–252.

P. Lader, A. Jensen, J. K. Sveen, A. Fredheim, B. Enerhaug, D. Fredriksson, Experimental investigation of wave forces on net structures, Applied Ocean Research 29 (2007) 112–127.

D. Van Nuffel, K. Vepa, I. De Baere, J. Rouck, W. Van Paepegem, J. Degrieck, Slamming wave impact on cylindrical structures: model tests including a rigid and deformable cylinder, in: Books of Abstracts of the Fourth International Conference on the Application of Physical Modelling to Port and Coastal Protection, Ghent, Belgium, 2012, pp. 109–110.

N. G. Jacobsen, D. R. Fuhrman, J. Fredsøe, A wave generation toolbox for the open-source CFD library: OpenFoam®, International Journal for Numerical Methods in Fluids 70 (2012) 1073–1088.

W. Wang, A. Kamath, C. Pakozdi, H. Bihs, Investigation of focusing wave properties in a numerical wave tank with a fully nonlinear potential flow model, Journal of Marine Science and Engineering 7 (2019) 375.

H. A. Schäffer, G. Klopman, Review of multidirectional active wave absorption methods, Journal of Waterway, Port, Coastal, and Ocean Engineering 126 (2000) 88–97.

H. Bihs, A. Kamath, M. Alagan Chella, Ø. A. Arntsen, Extreme wave generation, breaking, and impact simulations using wave packets in REEF3D, Journal of Offshore Mechanics and Arctic Engineering 141 (2019) 041802.

G. Zhu, Z. Shahroozi, S. Zheng, M. Göteman, J. Engström, D. Greaves, Experimental study of interactions between focused waves and a point absorber wave energy converter, Ocean Engineering 287 (2023) 115815.

G. Liu, Numerical simulation of waves in Shandong Laizhou Bay (in Chinese with English abstract), Express Water Resources & Hydropower Information 41 (2020) 57–60.

Y. Goda, Reanalysis of regular and random breaking wave statistics, Coastal Engineering Journal 52 (2010) 71–106.

1030 N. E. Huang, Z. Shen, S. R. Long, M. C. Wu, H. H. Shih, Q. Zheng, N.-C. Yen, C. C. Tung,
1031 H. H. Liu, The empirical mode decomposition and the Hilbert spectrum for nonlinear and
1032 non-stationary time series analysis, Proceedings of the Royal Society of London. Series A:
1033 Mathematical, Physical and Engineering Sciences 454 (1998) 903–995.

1034 E.-B. Lin, P. C. Liu, A discrete wavelet analysis of freak waves in the ocean, Journal of
1035 Applied Mathematics 2004 (2004) 379–394.

1036 Y. Ma, G. Dong, M. Perlin, S. Liu, J. Zang, Y. Sun, Higher-harmonic focused-wave forces on
1037 a vertical cylinder, Ocean Engineering 36 (2009) 595–604.

1038 N. Zhang, L. Xiao, H. Wei, Z. Cheng, G. Chen, Effects of static air gap and pontoon height
1039 on breaking wave impact loads on a fixed surface-piercing square column structure, Ocean
1040 Engineering 320 (2025) 120287.

1041 M. Farge, Wavelet transforms and their applications to turbulence, Annual Review of Fluid
1042 Mechanics 24 (1992) 395–458.

1043 B. Tai, Y. Ma, X. Niu, G. Dong, M. Perlin, Experimental investigation of impact forces
1044 induced by plunging breakers on a vertical cylinder, Ocean Engineering 189 (2019) 106362.

1045 P. Bonmarin, Geometric properties of deep-water breaking waves, Journal of Fluid Mechanics
1046 209 (1989) 405–433.

1047 R. J. Carini, C. C. Chickadel, A. T. Jessup, Surf zone waves at the onset of breaking: 2.
1048 predicting breaking and breaker type, Journal of Geophysical Research: Oceans 126 (2021)
1049 e2020JC016935.

1050 H.-J. Lim, K.-A. Chang, Z.-C. Huang, B. Na, Experimental study on plunging breaking waves
1051 in deep water, Journal of Geophysical Research: Oceans 120 (2015) 2007–2049.

1052 T. Cui, A. Kamath, W. Wang, L. Yuan, D. Han, H. Bihs, Focused plunging breaking waves
1053 impact on pile group in finite water depth, Journal of Offshore Mechanics and Arctic
1054 Engineering 144 (2022) 031202.

1055 J. R. Chaplin, R. C. T. Rainey, R. W. Yemm, Ringing of a vertical cylinder in waves, Journal
1056 of Fluid Mechanics 350 (1997) 119–147.

1057 Z. Tian, M. Perlin, W. Choi, Frequency spectra evolution of two-dimensional focusing wave
1058 groups in finite depth water, Journal of Fluid Mechanics 688 (2011) 169–194.

1059 J. Yu, X. Li, X. Zhang, H. Wang, X. Tian, X. Zhang, Numerical study on the hydrodynamic
1060 characteristics of a net plane under focused wave groups (in Chinese with English abstract),
1061 in: Proceedings of the 16th National Congress on Hydrodynamics & the 32nd National
1062 Conference on Hydrodynamics, Wuxi, Jiangsu, China, 2021, pp. 1305–1317.

1063 T. Cui, G. He, M. Jiang, W. Wang, L. Yuan, D. Han, A. Kamath, H. Bihs, Large eddy
1064 simulation of focused breaking waves with different wave steepness, Ocean Modelling 179
1065 (2022) 102122.

1066 G. Wang, T. Martin, L. Huang, H. Bihs, Modelling the flow around and wake behind net
1067 panels using large eddy simulations, Ocean Engineering 239 (2021) 109846.

1068 A. Kamath, M. Alagan Chella, H. Bihs, O. A. Arntsen, Breaking wave interaction with a
1069 vertical cylinder and the effect of breaker location, Ocean Engineering 128 (2016) 105–115.

1070 J. M. Esandi, E. Buldakov, R. Simons, D. Stagonas, An experimental study on wave forces
1071 on a vertical cylinder due to spilling breaking and near-breaking wave groups, Coastal
1072 Engineering 162 (2020) 103778.

1073 G. Wang, T. Martin, L. Huang, H. Bihs, Numerical investigation of the hydrodynamics of a
1074 submersible steel-frame offshore fish farm in regular waves using CFD, Ocean Engineering
1075 256 (2022) 111528.

1076 C.-W. Bi, Y.-P. Zhao, G.-H. Dong, Z.-M. Wu, Y. Zhang, T.-J. Xu, Drag on and flow through
1077 the hydroid-fouled nets in currents, Ocean Engineering 161 (2018) 195–204.

1078 Q.-P. Chen, C.-W. Bi, Z.-X. Zhang, Y.-P. Zhao, Hydrodynamic effect of different biofouling
1079 types on aquaculture netting, Ocean Engineering 279 (2023) 114430.